Review

Magnetic Particle Imaging in Oncology: Advances and Prospects for Tumor Progression Monitoring and Targeted Therapy

Panangattukara Prabhakaran Praveen Kumar *

Posted Date: 3 September 2025

doi: 10.20944/preprints202509.0352.v1

Keywords: magnetic particle imaging; SPIONS; tracers; cell tracking; cancer imaging; therapy

 doi:10.20944/preprints202509.0352.v1

Review

Magnetic Particle Imaging in Oncology: Advances and Prospects for Tumor Progression Monitoring and Targeted Therapy

Panangattukara Prabhakaran Praveen Kumar

Department of Biomedical Engineering, Institute for Quantitative Health Science and Engineering, Michigan State University, East Lansing, Michigan 48824, United States; pananga1@msu.edu; p4praveen.18@gmail.com

Abstract

Magnetic Particle Imaging (MPI) is a cutting-edge noninvasive imaging technique that offers high sensitivity, quantitative accuracy, and operates without the need for ionizing radiation compared to other imaging techniques. Utilizing superparamagnetic iron oxide nanoparticles (SPIONs) as tracers, MPI enables direct and precise visualization of target sites with no limitation on imaging depth. Unlike magnetic resonance imaging (MRI), which relies on uniform magnetic fields to produce anatomical images, MPI enables direct, background-free visualization and quantification of SPIONS within living organisms. This article provides an in-depth overview of MPI's applications in tracking tumor development and supporting cancer therapy. The distinct physical principles that underpin MPI, including its ability to produce high-contrast images devoid of background tissue interference, facilitating accurate tumor identification and real-time monitoring of treatment outcomes are outlined. The review outlines MPI's advantages over conventional imaging techniques in terms of sensitivity and resolution, and examines its capabilities in visualizing tumor vasculature, tracking cellular movement, evaluating inflammation, and conducting magnetic hyperthermia treatments. Recent progress in tracer optimization and magnetic navigation has expanded MPI's potential for targeted drug delivery along with deep machine learning procedures for MPI application. Additionally, considerations around safety and the feasibility of clinical implementation are also discussed in the present review. Overall, MPI is positioned as a promising tool in advancing cancer diagnostics, personalized therapy assessment, and noninvasive treatment strategies.

Keywords: magnetic particle imaging; SPIONS; tracers; cell tracking; cancer imaging; therapy

1. Introduction

Medical imaging has been fundamental to clinical diagnosis and treatment strategies for more than a hundred years, starting with the development of X-ray technology. Over time, diverse imaging methods like ultrasound, CT, PET-CT, SPECT, and MRI have become standard in healthcare [1,2]. These techniques are crucial for identifying diseases, tracking therapies, evaluating prognoses, and guiding medical procedures. Each imaging modality has distinct advantages and disadvantages, depending on the specific clinical need and the body part being examined. For instance, ultrasound is readily available and provides real-time images by detecting differences in tissue acoustic impedance. It is radiation-free and offers spatial resolutions of approximately 10–100 μm for superficial tissues and 1–2 mm for deeper structures. However, its utility is restricted for organs like the brain, lungs, or bones, and for small tumors less than 1 cm [3,4]. In contrast, PET-CT is highly effective for identifying early tumors or small metastatic lesions due to the precision of its molecular tracers, but it and SPECT use radioactive isotopes like ^{18}F-FDG and ^{99m}Tc, typically yielding moderate spatial resolutions of 5–7 mm [5]. MRI provides excellent soft tissue contrast and high spatial resolution of about 1 mm, with unlimited imaging depth, making it particularly valuable for neuroimaging [6]. However, its temporal resolution is limited, as image acquisition can take several

 doi:10.20944/preprints202509.0352.v1

minutes. Unique among current modalities, only PET and SPECT are inherently background-free, as they detect signals solely from injected tracers, allowing for clear "hot spot" visualization [7].

Magnetic Particle Imaging (MPI) is an innovative non-invasive imaging method developed to overcome challenges found in traditional imaging approaches [8,9]. Introduced in 2005 by Gleich and his team, MPI functions by generating specific areas where the magnetic field is nullified, referred to as field-free points or lines [10]. Within these regions, magnetic nanoparticles (MNPs) react to an oscillating magnetic field, generating detectable signals. MPI offers distinct benefits, such as the absence of background signals from biological tissues, the ability to penetrate deeply into tissues, and the capacity for precise linear quantification of tracer concentration, all without the use of ionizing radiation. The effectiveness of MPI, encompassing both its sensitivity and resolution, is directly influenced by the magnetic properties of the nanoparticle tracers [11]. However, current tracer options like Resovist and Feraheme have limitations, driving significant research toward creating more effective MPI agents [12]. Research efforts have focused on enhancing tracer performance through various strategies, including altering the composition with metal ion doping, precise control over particle size and shape, and developing specialized surface coatings to improve stability, distribution within the body, and magnetic responsiveness [13]. Advanced designs, such as Janus nanoparticles, are also being explored to combine multiple imaging functionalities, thereby compensating for the limitations of single imaging techniques [14,15]. Given that MPI tracers primarily circulate within the bloodstream, MPI is particularly well-suited for visualizing vascular conditions, including cardiovascular and cerebrovascular disorders, and shows considerable potential in cancer diagnosis and treatment (theranostics). MPI- based hyperthermia known as Magnetic Fluid Hyperthermia (MFH) is an emerging therapeutic field, in which SPIONS generate heat during the application of alternating magnetic field, which allow image guided tumor ablation by monitoring the temperature rise and allow to mark disease progression [16].

Recent advancements in nanoparticle design have significantly accelerated the progress of MPI, particularly in the creation of targeted and multifunctional tracers. This review offers a comprehensive overview of the foundational principles of MPI, details the evolution of various tracer types, and provides an in-depth analysis of contemporary innovations in tracer engineering. Our focus includes the critical aspects of chemical composition, physical characteristics, and surface modifications, all aimed at enhancing imaging performance. Furthermore, this review explores the diverse biomedical applications of MPI, drawing from recent literature to showcase its utility in both in vitro and in vivo settings [17]. A significant portion of our discussion is dedicated to the design strategies and therapeutic applications of MPI with integration to MFH, for potential clinical treatments. Finally, we address the current clinical challenges associated with implementing these advanced MPI and MFH techniques. By examining these hurdles, we aim to provide a realistic perspective on the translation of these promising technologies from research to practical clinical use, paving the way for future developments.

2. Brief Overview of Magnetic Particle Imaging (MPI)

MPI, first introduced in 2005, is an innovative imaging technology fundamentally linked to specific magnetic phenomena such as magnetic field gradients, the non-linear magnetization behavior of materials, and their saturation characteristics (Figure 1A) [8,18]. At its core, MPI operates by detecting the magnetic response of superparamagnetic iron oxide nanoparticles (SPIONS) after they are exposed to a rapidly oscillating magnetic drive field with sufficient energy. This induced magnetization is picked up by inductive receiver coils, and the resulting signal is interpreted through Faraday's law. The detected signal contains not only the primary drive frequency but also a series of harmonic frequencies, which are crucial for image formation and are separated using appropriate filtering during the signal reconstruction phase. A critical aspect of MPI is overcoming the suppression of harmonic generation in strong, time-constant magnetic fields, a phenomenon known as magnetic saturation. To circumvent this, a high-magnitude static magnetic gradient, typically ranging from approximately 1 to 7 T ($\mu 0^{-1}$ m^{-1}) is precisely superimposed. This creates a "Field Free

 doi:10.20944/preprints202509.0352.v1

Point" (FFP) (Figure 1B,C) or a "Field Free Line" (FFL) regions where the magnetic field is effectively zero. These FFPs or FFLs are then systematically shifted along a predefined scan trajectory to cover the entire imaging field of view (Figure 1A). As the FFP/FFL traverses through a sample containing nanoparticles, the distinct magnetic responses between the magnetically saturated (or semi-saturated) regions and the fully unsaturated (zero-field) regions enable the spatial encoding necessary for image reconstruction. The final images are generated using sophisticated visualization algorithms, primarily via two methods: either through a pre-obtained system matrix dataset, which maps the magnetic response of a single particle across every imaging voxel, or by the x-space method, which directly correlates the instantaneous signal obtained with the real-time location of the FFP/FFL (Figure 1D,E).

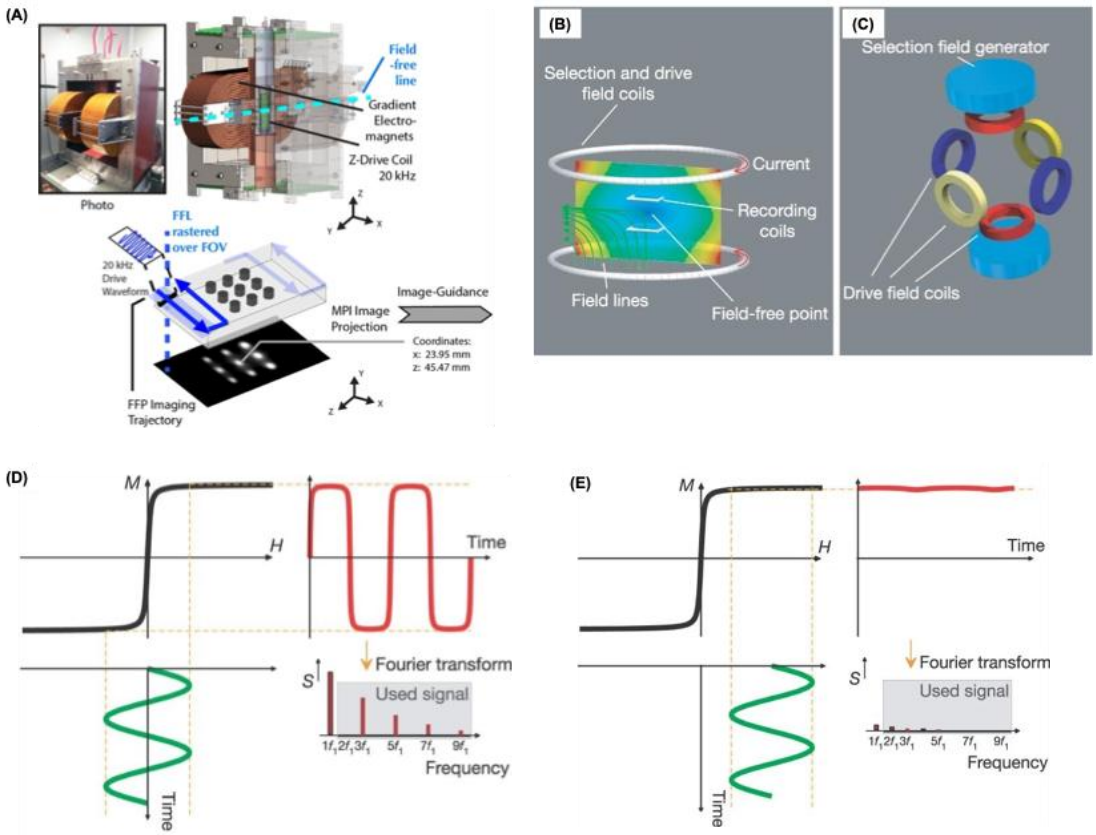

Figure 1. Principles and signal generation in magnetic particle imaging (MPI). (A) Schematic of the Berkeley MPI scanner setup. Image acquisition resembles projection scintigraphy, where magnetic nanoparticles traversing the field-free line (FFL) respond to an applied drive field (20 kHz, 20 mT). (B) Conceptual overview of a standard MPI scanner. Two large opposing rings generate a static selection field via d.c. currents, creating a central field-free point (FFP). The same rings also act as drive coils by superimposing a.c. currents on the d.c. field, while surrounding harmonic detection coils capture the particle response. (C) Design of an MPI system that encodes signals solely through drive fields. It incorporates dual selection field generators and three orthogonal pairs of drive coils to shift the FFP throughout the imaging volume. (D–E) Magnetization response of superparamagnetic particles. (D) Under an alternating magnetic field (H, green), the nonlinear magnetization (M, black) produces a time-dependent response (red) with distinct higher harmonics. (E) In contrast, a constant magnetic field drives the particles into saturation, yielding negligible harmonic content for image reconstruction (grey box). Reproduced with permission from [18], 2018 American Chemical Society and from [10], 2005, Springer Nature.

X-space is a sophisticated theoretical framework used to map the concentration distribution of nanoparticles in MPI. It employs a reconstruction algorithm where the resulting image is modeled as a convolution of the nanoparticle spatial distribution with a normalized point spread function (PSF). The PSF describes how signal strength changes relative to distance from a point source and is

 doi:10.20944/preprints202509.0352.v1

mathematically derived as the first derivative of the Langevin function. This derivative is essential because MPI detects only changes in magnetization, which are captured by the receiver coil.

The MPI signal is mainly influenced by fixed machine parameters such as gradient strength (G) and the magnetic behavior of the tracer, represented by its magnetization curve (dM/dH). Improved imaging performance is associated with a higher peak and narrower full width at half maximum (FWHM) of this curve. Key tracer properties impacting MPI quality include magnetic moment (μ), coercivity (Hc), saturation magnetization (Ms), relaxation time (τ), magnetic susceptibility (χ), and magnetocrystalline anisotropy (K), which also affects thermal response. While the point spread function (PSF) shape defines basic system resolution, imaging sensitivity and clarity also rely on tracer relaxation mechanisms either Néel (τN) or Brownian (τB) that describe delays in magnetization alignment with the excitation field. Specifically, Néel relaxation, governed by the equation $\tau N = \tau 0 \exp(KAV/kBT)$, depends on the anisotropy constant (KA) and nanoparticle volume (V), indicating that both particle size and anisotropy are critical to magnetic nanoparticle performance in MPI.

3. Commercial Tracers for MPI

MPI tracers can be evaluated directly with an MPI scanner, such as the Magnetic Insight MOMENTUM, or indirectly using characterization tools like the magnetic particle spectrometer (MPS) and magnetic particle relaxometer (MPR). These benchtop methods provide rapid screening of tracer properties but do not fully replicate scanner conditions. MPS employs only an alternating magnetic field (AMF) to probe the nonlinear magnetization of nanoparticles and measures the resulting excitation frequency and harmonic spectrum. This harmonic profile provides information about both tracer sensitivity and resolution. MPR, by contrast, extends the MPS method by adding a time-varying bias field that simulates movement of the field-free region (FFR) in an MPI scanner [19]. This enables evaluation of relaxation phenomena that MPS alone cannot capture [20,21]. While useful, both approaches lack the magnetic gradient fields essential for spatial encoding in MPI and therefore cannot directly reproduce scanner performance. The primary tracer metrics are sensitivity and resolution. In x-space MPI, sensitivity is typically reported as signal intensity normalized to iron or magnetite mass, while resolution is quantified as the full width at half maximum (FWHM) of the point-spread function (PSF). The PSF is obtained by plotting measured signal versus applied field, and comparing PSFs of different tracers can reveal performance variations (Figure 2A) [22,23]. Dilution series are also commonly used, where the slope of signal intensity versus tracer concentration provides specific signal intensity and can define the tracer's detection limit (Figure 2B). Additionally, 2D MPI scans can be performed with equal iron content samples to directly compare maximum intensity across tracers (Figure 2C) [22]. Measurement outcomes are highly dependent on experimental parameters, including AMF frequency and amplitude, gradient strength in scanners, and bias fields in relaxometers. A key observation is the trade-off between resolution and sensitivity: higher AMF amplitudes enhance sensitivity but reduce resolution, whereas lower amplitudes favor sharper resolution but weaker signals. Because MPS and MPR do not account for image acquisition or reconstruction processes, their data cannot be directly translated to scanner results [23].

A wide range of magnetic nanoparticles has been introduced into the market and subsequently explored as tracers for MPI. Interestingly, most of these particles were not originally designed for MPI but for other biomedical purposes, including iron supplementation therapies and magnetic resonance imaging (MRI) contrast enhancement. As a result, their performance in MPI is often less than ideal, although they are still widely employed as reference standards for evaluating the sensitivity and efficiency of newly developed tracers. One of the earliest examples is Resovist, a carboxydextran-stabilized magnetite formulation that received clinical approval as an MRI agent [10,24]. While its superparamagnetic iron oxide cores are relatively small (3–5 nm), particle–particle interactions create a fraction of effectively larger magnetic domains (25–30 nm), which enhances its MPI signal [25]. A related formulation, Ferucarbotran, has the same composition as of Revovist and is marketed off-label, while VivoTrax represents a rebranded version of ferucarbotran sold specifically for MPI applications [26]. More recently, VivoTrax+ has been introduced, incorporating

 doi:10.20944/preprints202509.0352.v1

magnetic fractionation to enrich the subset of particles with stronger responses, thereby improving image resolution and signal specificity [27,28]. Another noteworthy example is Feraheme (ferumoxytol), a carboxymethyldextran-coated nanoparticle originally approved for iron deficiency therapy, which is also used experimentally in MRI [29]. However, head-to-head comparisons indicate that its MPI sensitivity and resolution are inferior to those of VivoTrax. Beyond these formulations, newer clustered systems such as Perimag and Synomag-D which were characterized by larger hydrodynamic sizes (30-50 nm) with a dextran shell of 130 nm [30,31]. These tracers possess higher magnetic responsiveness demonstrate superior MPI performance relative to Resovist and VivoTrax. PrecisionMRX nanoparticles, in contrast, are engineered as monodisperse 24-nm systems with customizable surface coatings, distinguishing them from the broader polydisperse aggregates of conventional formulations, though their MPI characteristics remain in a similar range [30]. While tabulated data on these agents provide useful comparisons of particle size, linewidth, and sensitivity, it should be noted that many measurements derive from magnetic particle relaxometry rather than direct MPI scans, which can yield differing outcomes. Collectively, the contrast between these commercial products and specialized, laboratory-engineered tracers highlights the substantial opportunities that remain for tailoring nanoparticle design to optimize MPI performance [32]. For consistency, widely available commercial nanoparticles are often used as reference materials to benchmark new tracers. Such comparisons allow researchers to normalize results across different instruments and studies, providing a reliable baseline for evaluating tracer improvements. **Tabel 1** represents the commercially available MPI tracers with their sensitivity, and magnetic properties.

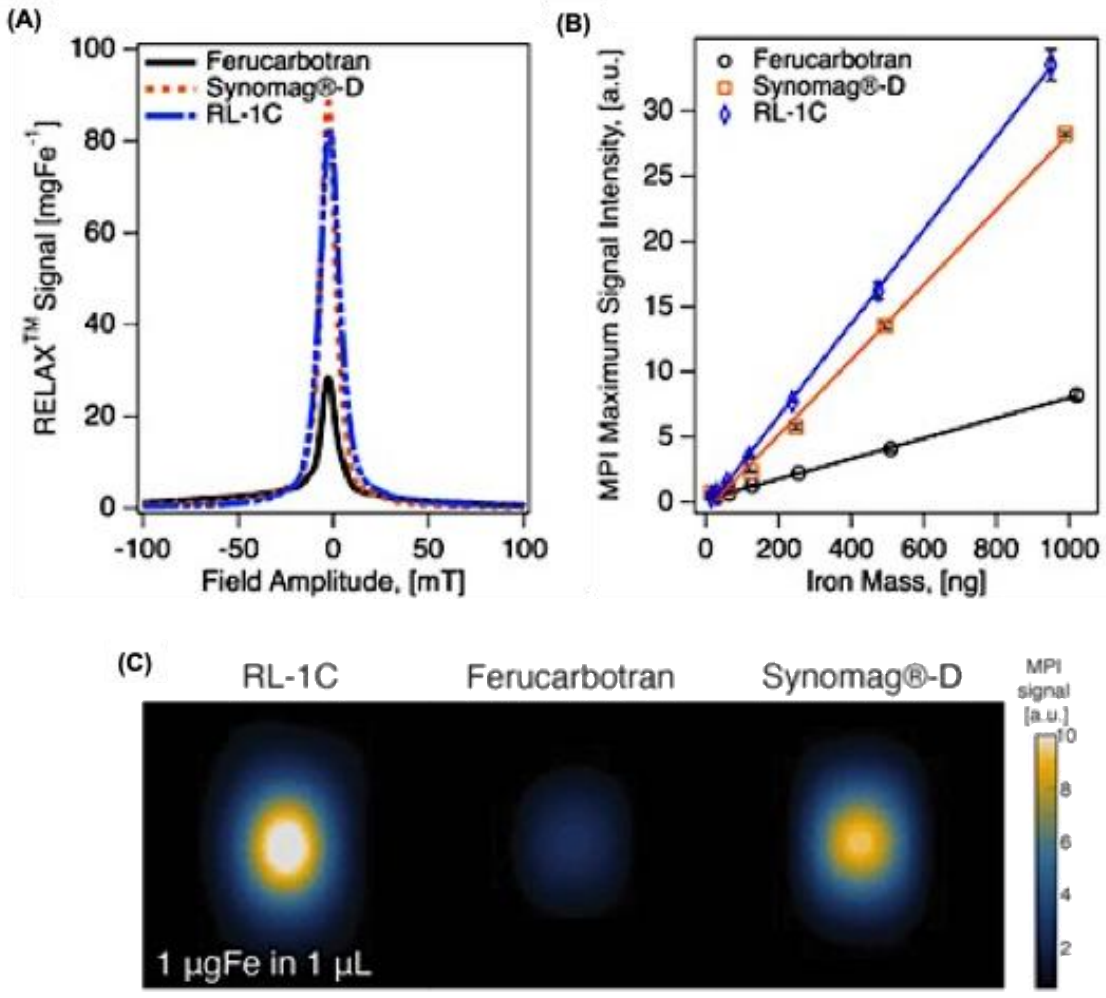

Figure 2. MPI performance of commercial tracers compared with RL SPIONs. (A) Point spread function (PSF) acquired with the relaxometry module of the MOMENTUM™ scanner, illustrating the signal characteristics of the SPIONs. (B) Serial dilution experiments demonstrate a linear correlation between iron content and MPI

 doi:10.20944/preprints202509.0352.v1

signal intensity across all three tracers in 2D high-sensitivity mode. (C) Two-dimensional MPI maximum intensity projections of 1 mgFe in 1 µL solution for each tracer. Reproduced with permission from [22], 2021 Ivyspring publishers.

Table 1. Summary of various commercially available MPI tracers.

Tracer	Diameter	Magnetic diameter	FWHM	Sensitivity	System used	Frequency and gradient	Ref
Resovist	4	n.r	9.6 mT	13.74 (mV/mgFe)	MPR	20 kHz, 20 mT	[30,33]
VivoTrax	4.2	n.r	11.4 mT	8.83 (mV/mgFe)	MPR	20 kHz, 20 mT	[30]
VivoTrax+	n.r	n.r	7.9 mT	2.4x VivoTrax	MOMENTUM	n.r	[28]
Ferucarbotran	9.6	7.6, 22.1*	11.2 mT	25.8 (a.u./mgFe)	MOMENTUM	45 kHz, 16 mT, 5.7 T/m	[22]
Synomag-D	28.6	8.2, 19.3*	9.2 mT	87.8 (a.u./mgFe)	MOMENTUM	45 kHz, 16 mT, 5.7 T/m	[22,31]
Feraheme	6–7	n.r	39.5 mT	2.12 (mV/mgFe)	MPR	20 kHz, 20 mT	[30,34]
PrecisionMRX	24.4	n.r	12.4 mT	13.89 (mV/mgFe)	MPR	20 kHz, 20 mT	[30]
Perimag	Clustered / n.r	n.r	7.3 mT	29.49 (mV/mgFe)	MPR	20 kHz, 20 mT	[30]

n.r : not reported. The magnetic size was obtained by applying a bimodal lognormal distribution fit, yielding average diameters corresponding to two distinct particle populations.

4. Tracer Characteristics and Their Correlation with MPI Performance

In MPI, spatial resolution is defined as the ability to distinguish two signals of equal intensity and is primarily influenced by the instrument's magnetic gradient strength and the physical properties of the SPION tracers. Stronger gradients narrow the field-free region, while nanoparticles with narrower PSFs yield higher resolution [35]. Optimized SPIONs not only enhance image quality but can also reduce instrument costs, as improved tracers permit lower gradient requirements [36]. Sensitivity, another critical performance factor, reflects the capacity to detect minute tracer amounts and is essential for applications such as cell tracking. It is determined by signal intensity in the PSF and the Langevin curve response, and can be improved through both hardware advances, such as coil design, and tracer development, particularly by enhancing saturation magnetization. With continued progress, MPI sensitivity has the potential to approach that of nuclear imaging techniques. MPI harnesses SPIOs as tracers, with their performance particularly signal sensitivity and spatial resolution being critically dependent on nanoparticle size, shape, and surface chemistry [37]. The precise engineering of these tracers is essential for MPI's broad biomedical applications, ranging from noninvasive cell tracking and vascular imaging to the detection and characterization of tumors [12].

 doi:10.20944/preprints202509.0352.v1

4.1. Size Correlation of SPIONS

The magnetic core diameter plays a crucial role in determining the overall efficiency of SPION-based tracers. For single-core nanoparticles, both sensitivity and spatial resolution scale roughly with the cube of the core size, largely due to the increase in saturation magnetization (Ms) [38,39]. However, as highlighted by Tay and colleagues, this enhancement reaches a limit; larger cores experience stronger Brownian relaxation effects and a gradual transition from superparamagnetism to superferromagnetic iron oxide NPs (SFMIOs), which reduces magnetic responsiveness [40]. This constraint, often referred to as the "Langevin wall," leads to a decline in Ms and restricts further performance gains. Experimental studies suggest that an optimal single-core SPION diameter for balancing resolution and sensitivity lies between 24 and 28 nm. Supporting this, Shel et al. evaluated several commercial SPION formulations and confirmed that both imaging resolution and tracer sensitivity are strongly dependent on particle size [41].

Studies have shown that nanoparticle tracers with carefully tuned properties can significantly improve MPI performance. For example, particles with an average core diameter of about 20 nm, a narrow log-normal size distribution ($\sigma v \approx 0.26$), and a hydrodynamic size near 30 nm yielded optimal results at an excitation frequency of 25 kHz [39]. Under these conditions, they produced signal intensities roughly four times higher and spatial resolution about 20% better than conventional MRI contrast nanoparticles. In general, smaller nanoparticles are advantageous for circulation and biocompatibility, although they often generate weaker signals. Larger particles, on the other hand, can enhance signal output and resolution but require precise control to prevent aggregation or excessive magnetic relaxation, both of which broaden the size distribution and diminish image quality. The superior behavior of larger magnetic nanoparticles (MNPs) at lower frequencies such as 25 kHz is explained by the extended measurement time window, which allows their magnetization to more effectively follow the applied magnetic field. However, once the median particle size surpasses ~20 nm under these conditions, signal intensity begins to decline due to relaxation delays, which impair spatial resolution. Both the magnetic core and the surrounding coating layer play critical roles in MPI efficiency. When the distribution is kept narrow, increasing the core size tends to improve signal characteristics. Experimental and computational studies consistently indicate that highly uniform, single-core iron oxide nanoparticles with diameters in the 26–27 nm range (±1.5 nm) deliver excellent MPI performance, aligning well with theoretical predictions that place the optimal diameter between 25 and 30 nm [32].

4.2. Shape Characteristics of SPIONS

Nanoparticle shape plays a crucial role in determining magnetic behavior and imaging quality in MPI. Spherical single-core particles provide uniform magnetization, producing sharp PSFs and reliable image reconstruction. In contrast, multicore or anisotropic designs can boost signal output but demand careful engineering to avoid signal broadening from interparticle interactions. Effective tracer design therefore hinges on precise control of size, shape, and surface chemistry to achieve optimal sensitivity, resolution, and reproducibility under alternating magnetic fields.

In of the studies Nigam et al. show cased that dextran coated rod shaped iron oxide nanoparticles outperform than spherical and vivotrax (VTX) for MPI application [42]. The nanorods exhibited dramatically enhanced MPI performance compared to VTX and SPIONPs, showing 10–15× higher signal intensity and better resolution due to their shape anisotropy and magnetic alignment along the nanorods' long axis. While none of the particles resolved wells closer than 1.5 mm, simulations confirmed that nanorod length and concentration directly influence MPI signals, suggesting potential for improved tracer design in drug delivery and theranostics for lung manifestations.

A specialized MPI tracer, CIONs-22 (cubic iron oxide nanoparticles with a 22 nm edge length), has been developed by wang et al. through careful engineering of nanoparticle size and shape in accordance with MPI physics [38]. This cubic geometry is crucial as it leads to a lower proportion of disordered surface spins, resulting in significantly higher saturation magnetization compared to

 doi:10.20944/preprints202509.0352.v1

spherical nanoparticles. This enhanced magnetic property, combined with a smaller coercivity than larger cubic nanoparticles, directly translates to superior sensitivity and resolution in MPI. CIONs-22 exhibit efficient cellular uptake and significantly outperform commercial tracers like VTX in stem cell labeling and tracking, demonstrating their potential. Their unique magnetic characteristics and effective cellular integration enable precise, real-time, and prolonged monitoring of stem cells in preclinical models, such as hindlimb ischemia mice. This advancement positions CIONs-22 as a promising tool to accelerate the development and clinical application of stem cell therapies by providing unprecedented insights into their in vivo dynamics. In another study Sahitya et al. showed that among the various nanocube based structures, the one with short nanocube chain assemblies exhibit remarkable MPI signal enhancement of 57% with respect to the individually dispersed or the centrosymmetric cluster analogues, and 36% higher than VTX [26]. The uniaxial magnetic dipolar coupling occurring in the chain-like nanocube assembly enhanced the MPI and MRI properties. Moreover, the study highlighted when the nanocube clusters expose to lytic enzyme, the shorter nanocubes formed possess enhanced MPI response and high magnetic hyperthermia effect.

Recent advances in magnetic nanoparticle design have led to the creation of iron oxide nanoworms and nanochains, aimed at overcoming the limitations of conventional spherical particles. These structures enhance MPI by providing sharper resolution and stronger signals, supporting applications in cancer diagnostics and real-time cell tracking. Nanoworms are biocompatible iron oxide structures made by methods like coprecipitation of Fe^{2+} and Fe^{3+} or a modified heat-up process using iron oleate [43]. They form when spherical nanoparticles aggregate, influenced by weak surface ligands such as trioctylphosphine oxide [44]. While their diameters match the starting spheres, their lengths typically range from 50–200 nm. Both spheres and nanoworms share a maghemite crystal structure but differ magnetically spheres are superparamagnetic, while nanoworms show ferromagnetism. Dextran-coated nanoworms have been investigated for tumor imaging and targeting [45]. Techniques like high-resolution TEM reveal their magnetic structure under strong fields. Nanoworms linked with indocyanine green serve as promising contrast agents for multimodal breast cancer imaging, providing strong tumor-to-normal tissue contrast across MPI, NIR fluorescence, and photoacoustic imaging [46].

A novel approach to tracer design has recently emerged, utilizing strong magnetic dipole–dipole interactions between particles that align to form nanoparticle chains in fluid under the influence of an external magnetic field. This self-assembly process significantly amplifies the local magnetic field by nearly an order of magnitude leading to much sharper PSFs. Using this strategy, Tay and colleagues reported remarkable enhancements, including up to a 40-fold increase in sensitivity and a tenfold improvement in spatial resolution, which theoretically enables real-time tracking of individual cells in vivo (Figure 3A-C) [47]. Subsequent investigations into this “chaining hypothesis” have focused on factors that regulate the dynamics of chain formation. For instance, Fung and co-workers emphasized that rapid chain assembly requires low-viscosity environments since higher viscosities hinder particle mobility and elevated nanoparticle concentrations, which minimize inter-particle distances and promote efficient dipole interactions (Figure 3D) [48]. They tested this by diluting and sonicating polarized SFMIOs. After a 10-fold dilution, they still showed superferromagnetism (Figure 3E), indicating that chains remain intact despite dilution. If dissolution had occurred, this behavior would not be observed. In contrast, sonication restored superparamagnetism (Figure 3F), confirming chain breakage. Since sonication applies strong localized energy via cavitation, such dissolution is unlikely during MPI scans. The behavior of chain-like tracers has been further explored through computational modeling. Zhao and colleagues used simulations to examine how magnetic dipole–dipole interactions influence both MPI performance and the dynamic magnetization of particles arranged in chains [49]. Their findings revealed that chains containing two or more nanoparticles can significantly improve signal strength and resolution, consistent with experimental reports by Tay et al. [47]. Moreover, the study highlights a broad design space for optimizing MPI tracers by adjusting factors such as chain length, interparticle spacing, nanoparticle composition, and solution viscosity. Novel designs like iron oxide nanochains

 doi:10.20944/preprints202509.0352.v1

(FeONCs), optimized for breast cancer imaging, further outperform spherical, cubic, and nanoworm tracers in terms of magnetic properties was reported by kumar et al. [50]. Magnetic relaxometry confirms FeONCs offer superior sensitivity compared to standard tracers such as VivoTrax, Synomag D50 and D70.

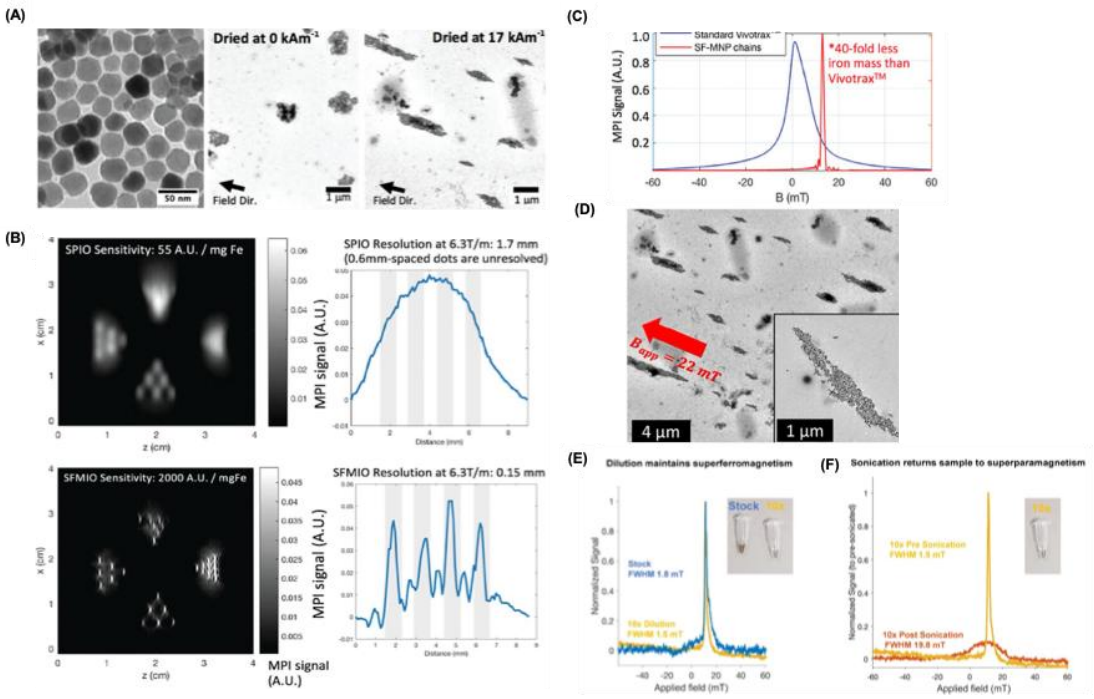

Figure 3. Linear microscale nanochain formation and its MPI response. (A) Transmission electron microscopic (TEM) images for microscopic linear chain formation application of an external magnetic field (Blacked arrow indicate the applied magnetic field direction). (B) MPI phantom images for SFMIONs made from 0.3 mm radii wells with varying well-to-well spacing (mm). (C) Enhanced PSF in x-space reconstruction was observed, with SFMIONs chains exhibiting approximately 40 times higher signal intensity and a tenfold increase in spatial resolution compared to the MPI reference tracer, Vivotrax. (D) TEM images for SFMIOs chain formation under magnetic field. Red arrow indicates the direction for field application. (E) and (F) represents the SFMIONs response for MPI under two different conditions such as dilution (E) and sonication (F) of the SPIONS. Inset shows the physical appearance of SFMIONs after the dilution and sonication process respectively. Reproduced with permission from [47], 2021, Wiley publishers and [48], 2023, American Chemical Society.

4.3. Role of Surface Coatings on SPIONS

Surface coatings are vital for maintaining the performance of MPI tracers in biological environments. They play multiple roles: stabilizing nanoparticles, modulating magnetic properties, and influencing imaging outcomes. Coatings such as gold shells, silica, or crosslinked polymers can stabilize nanoparticles by reducing aggregation and counteracting van der Waals forces that would otherwise cause clustering of NPs [17,51]. Beyond stabilization, these coatings can directly impact the magnetic behavior of the nanoparticle cores. For example, gold shells or ferromagnetic outer layers can enhance the magnetic moment, improving signal intensity without increasing the amount of magnetic material [51].

Non-magnetic coatings, while useful for biocompatibility and stability, may reduce the saturation magnetization per core, which in turn affects the sensitivity of MPI measurements. For instance, in one of the studies it has reported that applying a crosslinked polymer layer to SPIOs can alter their MPI performance [52]. The crosslinked single-core SPIONs, with an average core size of 18 nm and designated PF127DAPG, demonstrated a higher signal-to-noise ratio (SNR) and, as a result, improved spatial resolution compared to the non-crosslinked PF127 nanoparticles. Consequently, achieving the same spatial resolution required 5.3 µg of iron for PF127 SPIONs, whereas only 1.3 µg

 doi:10.20944/preprints202509.0352.v1

of iron was sufficient for PF127DAPG SPIONs. Non-magnetic coatings tend to reduce the saturation magnetization of the nanoparticle cores, thereby modifying their magnetic behavior. The properties of these coatings can strongly influence MPI signals through dynamic magnetic relaxation processes. In particular, the Néel relaxation time which is vital for MPI sensitivity is highly dependent on the nature of the nanoparticle surface layer. Additionally, studies have demonstrated that silica (SiO_2) coatings on zinc ferrite ($Zn_{0.4}Fe_{2.6}O_4$) nanoparticles improve signal-to-noise ratios in magnetic particle spectroscopy relative to uncoated particles, even though the thickness of the silica shell has only a minor effect on the magnetic particle signal itself [53]. This enhanced signal stability, especially in environments such as PBS, can substantially increase MPI sensitivity and broaden the practical use of these tracers.

Surface coatings play a significant role in determining the spatial resolution of MPI. Some reports indicate that gold coatings do not substantially alter the magnetic characteristics that affect image quality, whereas other studies show that certain coatings can enhance nanoparticle resolution [54]. The properties of the magnetic core, combined with the attributes of the surrounding non-magnetic shell in core–shell nanoparticles, influence MPI signals via dynamic relaxation, thereby affecting resolution [55,56]. When tuning the core size of magnetic nanoparticles for MPI, relaxation effects become prominent for diameters above roughly 28 nm, although the precise threshold depends on the applied magnetic field and the coating material. Additionally, larger nanoparticles and strong interparticle interactions can hinder colloidal stability and monodispersity in aqueous solutions, which can indirectly reduce imaging resolution [56].

4.4. Alternatives to SPIONs as MPI Tracers

Most MPI tracers have traditionally been based on FeONPs, but alternative magnetic nanoparticles (MNPs) are emerging as promising options, though research in this area is still limited. In principle, any biocompatible MNP with superparamagnetic behavior and high saturation magnetization (Ms) could serve as an effective MPI contrast agent.

Pure FeONPs, for example, can achieve very high Ms values (up to 176 emu/g at 13 nm), but their poor chemical stability limits imaging applications. They oxidize rapidly in air, necessitating stabilizing coatings. Gloag et al. developed single-core iron nanoparticles with an iron oxide shell and polymer brush coating, which prevented oxidation and maintained colloidal stability for over eight weeks (Figure 4A) [57]. These 14 nm particles exhibited a Ms of 166 emu/g and produced MPI signals ~80% that of larger multi-core VivoTrax particles, outperforming similarly sized SPIONs (Figure 4B,C). Their strong MPI response at small sizes opens opportunities for cellular and brain imaging that were previously challenging.

Metal alloy MNPs have recently attracted attention for their potential in MPI applications. Among these, FeCo alloy nanoparticles are particularly notable, exhibiting very high saturation magnetization (Ms) values, reaching up to 215 emu g^{-1} (Figure 4D)[58]. Additionally, they retain superparamagnetic properties at sizes below 20 nm, highlighting their suitability for MPI [59]. Like pure iron nanoparticles, FeCo MNPs require stabilization to prevent oxidation when exposed to air. In a recent study, Song et al. produced 10 nm FeCo nanoparticles coated with graphitic carbon and PEG (Figure 4E) [60]. These coated nanoparticles demonstrated exceptional MPI signal strength 6.08 times higher than that of VivoTrax at comparable molar core concentrations (Figure 4F). The graphitic carbon layer effectively protects the reactive FeCo core from rapid oxidation. Other alloyed nanoparticles, such as FePt (Ms = 100 emu g^{-1}) [61]and Fe_5C_2 (Ms = 125 emu g^{-1}) [62], also show promise for MPI, though they have yet to be explored in this context.

 doi:10.20944/preprints202509.0352.v1

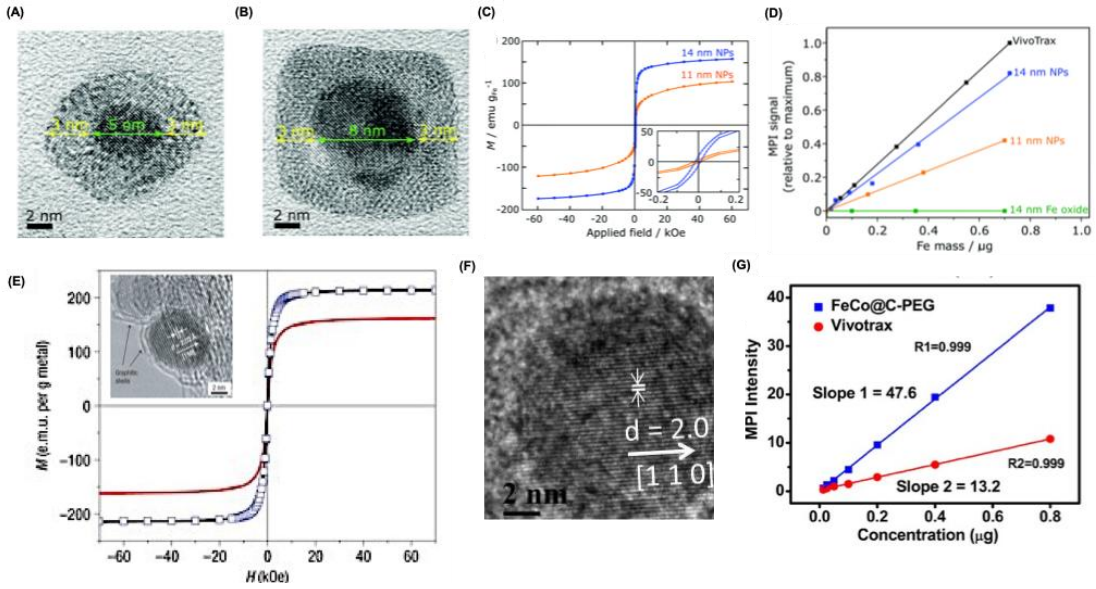

Figure 4. Alternative structures for MPI application. (A-B) High resolution transmission (HR-TEM) microscopy images for core-shell FeONPs with diameter 11 and 14 nm respectively. (c) Magnetic hysteresis curves showing the field-dependent magnetism of Core-shell nanoparticles at 300 K. (D) Plot of MPI signals relative to commercial VivoTrax as a function of Fe mass in the core-shell NPs. (E) Magnetization field measurements at room temperature on FeCo/graphitic-shell nanocrystals of approximately 7 nm (black curve) and 4 nm (red curve) soon after synthesis. For the ~7 nm nanocrystals, additional data collected after one month of exposure to ambient conditions (blue markers) showed no noticeable change compared to the initial results (solid black curve). The absence of hysteresis in the solid curves, obtained by cycling the magnetic field, confirms the superparamagnetic behavior of these nanocrystals. Inset shows the HRTEM images for nanocrystals. (F) HRTEM images for Carbon-coated FeCo nanoparticles. (G) MPI response for Carbon-coated FeCo nanoparticles and Vivotrax with varying Fe content. Reproduced with permission from [57], 2020, RSC publishers and from [58,60], 2006, 2020, Nature Publishers.

Ferrites with the general formula $MxFe_{3-x}O_4$ adopt a spinel crystal structure, where M represents a divalent transition metal ion. In conventional Fe_3O_4-based SPIONs, this position is occupied by Fe^{2+}. Introducing other divalent metal ions into the lattice can modify the magnetic characteristics of the nanoparticles, potentially enhancing their performance in MPI. In such doped ferrites, Fe^{2+} ions are partially replaced by ions such as Zn^{2+}, Co^{2+}, or Mn^{2+}. However, for biomedical applications, the biocompatibility and toxicity of these materials remain critical considerations. In a recent study, Silvestri and colleagues produced cubic ferrite nanoparticles with controlled amounts of Co and Zn doping and assessed their MPI behavior [63]. High-quality Co-ferrite nanocubes were initially prepared via a non-hydrolytic synthesis method. By varying the metal precursors, cobalt ions could be partially replaced with zinc, forming mixed Zn–Co ferrites, or fully substituted to yield pure Zn-ferrite nanocubes, all with sizes below 15 nm. Among these, Zn-ferrite cubes demonstrated the best MPI performance, exhibiting the narrowest full width at half maximum (FWHM) and the highest signal-to-noise ratio (SNR). Notably, compared to the commercial tracer VivoTrax, Zn-ferrite nanocubes achieved an SNR three times higher, whereas Co-ferrite cubes produced nearly no detectable MPI signal. Given their superior imaging properties and generally higher biocompatibility relative to Co-ferrites reflected in the greater safe daily intake of Zn-ferrite nanoparticles emerge as particularly promising MPI tracers. These advantageous properties of Zn-ferrites have been consistently reported in other recent studies [64,65] .

Multicore nanoparticles have garnered attention for their potential in MPI. For instance, the commercial multicore tracer Synomag has demonstrated roughly threefold higher sensitivity compared to Resovist in traveling wave MPI measurements. Kratz and colleagues synthesized multicore particle (MCP 3) tracers via coprecipitation, which exhibited about five times the

 doi:10.20944/preprints202509.0352.v1

performance of Resovist in magnetic particle spectroscopy and phantom MPI scans using the Bruker MPI system [66,67]. More recently, core–shell nanoparticles, such as magnetite-gold structures, have been investigated as multimodal imaging agents. The presence of a gold shell is reported to slightly reduce saturation magnetization while marginally increasing both the effective magnetic diameter and MPI signal intensity, likely due to interactions at the interface of the magnetite core and gold shell [51].

Efforts have also been made to design composite nanoparticles for MPI-based applications. Janus nanoparticles, for example, were created by embedding iron oxide cores into semiconducting polymers, achieving three times the sensitivity of Vivotrax for cell tracking studies [14]. Additionally, genetically engineered magnetotactic bacteria have been explored as living multimodal contrast agents capable of both MPI and bioluminescence imaging [68]. For drug delivery and MPI quantification, composites consisting of magnetite cores coated with doxorubicin-loaded PLGA have been formulated [69]. Other examples include Synomag-D particles encapsulated in red blood cells to extend circulation time [70], as well as artificial chylomicrons used for assessing lipid uptake [71]. Collectively, these studies highlight the potential of combining MPI with complementary biomedical applications and suggest further opportunities for enhancing imaging performance through multimodal nanoparticle designs.

5. Application of MPI in Oncology

5.1. Cell Tracking

In biomedical research, MPI has been applied to monitor the migration, distribution, and persistence of various cell types, including immune cells (T cells, macrophages, dendritic cells) and stem cells, following adoptive transfer [41,72]. Cells can be labeled ex vivo with SPIONs without affecting viability or function, allowing accurate, longitudinal quantification of cell localization. MPI offers advantages over traditional imaging techniques such as MRI or radionuclide imaging by providing true quantitative data, fast imaging, and zero ionizing radiation exposure, making it a promising tool for evaluating cell-based therapies and immune responses in real time.

5.1.1. Tumor Cell Tracking

The first reported application of MPI for cancer was an in vitro study in 2014 by the University Hospital of Schleswig Holstein and the University of Luebeck, Germany [73]. Dextran-coated SPIONs (UL-D) were synthesized and efficiently internalized by head and neck squamous cancer cells, producing strong MPI signals in vitro. While in vivo imaging was not performed, the study confirmed that labeling cells with UL-D nanoparticles did not affect mitochondrial activity, viability, proliferation, cytokine secretion, or reactive oxygen species production, suggesting minimal impact on tumor behavior. In 2016, another in vitro study showed that MPI-compatible monodisperse iron oxide nanoparticles could detect cancer-specific proteases via changes in their Magnetic Particle Spectrum (MPS) [74]. Peptide-linked nanoparticles exhibited measurable spectral shifts upon exposure to proteases. Although not yet validated in vivo, this approach could enhance MPI specificity for cancer detection. Further improvements in sensitivity may be achieved by optimizing magnetic core size and using pulsed MPI excitation instead of continuous-wave excitation.

MPI is widely used for tracking immortalized cancer cells [41]. Son et al. developed MPI-tailored SPIONs (14 nm) via thermal decomposition, conjugated with poly(styrene-co-maleic anhydride), and hydrolyzed to yield Fe_3O_4–COOH NPs (Figure 5A) [14]. These NPs exhibited an MPI signal three times stronger than Vivotrax and seven times stronger than Feraheme at equal Fe concentrations (Figure 5B). For multimodal imaging, they were labeled with PFODBT dye, maintaining similar MPI performance as that of Fe_3O_4–COOH NPs (Figure 5C). HeLa cells incubated with Fe_3O_4@PFODBT–COOH NPs (60 μg Fe/mL) for 4 h showed red perinuclear fluorescence, and enhanced MPI signals confirming the cellular uptake (Figure 5C,D). ICP-MS quantified ~31 pg Fe per cell, and MTS assays

 doi:10.20944/preprints202509.0352.v1

indicated no cytotoxicity up to 48 h, demonstrating excellent biocompatibility for cell-labeling applications.

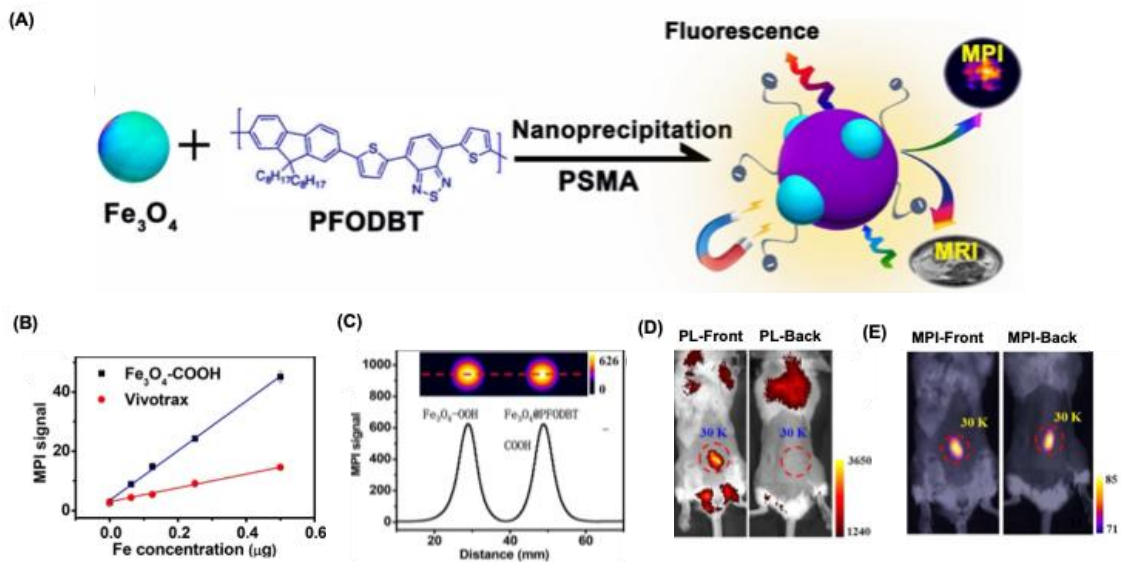

Figure 5. Application of MPI for cell tracking and muti mode imaging. (A)A schematic for the preparation of FeONPs tracer with multimode imaging capability. (B) MPI signal intensity comparison for Fe_3O_4-COOH and Vivotrax for varying Fe concentration in water. (C) Two-dimensional projection MPI was performed on Fe_3O_4–COOH and Fe_3O_4@PFODBT-COOH samples, each containing 8 μg of iron dispersed in 200 μL of water. (D) Fluorescence imaging of mice captured from both anterior and posterior views following subcutaneous administration of Fe_3O_4@PFODBT-COOH–tagged cells (excitation at 540 nm, emission at 680 nm). (E) Corresponding two-dimensional projection MPI scans from the same front and back perspectives after injection of the labeled cells. Reproduced with permission from [14], 2017, American Chemical Society.

Melo and colleagues evaluated the performance of micron-sized iron oxide particles (MPIOs) against the widely used VivoTrax (Magnetic Insight Inc.) for labeling and tracking iron-tagged cancer cells in a mouse brain model [75]. Unlike conventional SPIONs, MPIOs are composed of numerous small cores (~5–10 nm) embedded within a polystyrene matrix. This clustered architecture allows the particles to behave as a single large superparamagnetic core (~0.9 μm), generating significantly enhanced MPI signals. As a result, MPIO-labeled cells were detected and quantified more efficiently in vivo than cells labeled with VivoTrax, highlighting the potential of MPIOs for sensitive MPI-based cell tracking. MPIONs were further utilized to track circulating tumor cells (CTCs), with both MPI and MRI providing complementary insights into tumor cell distribution from primary to distant sites and monitoring SPION dilution during cell proliferation. These studies collectively demonstrate the versatility of MPIONs as a robust tracer for longitudinal, quantitative imaging of cancer cells in vivo. Building on this, Makela et al. employed MPIONs to monitor tumor cell metastasis in a breast cancer model using MPI in combination with CT and bioluminescence imaging [76]. 4T1BGL cells labeled with MPIONs were administered into the mammary fat pad of mice, and tumor progression was tracked using 3D MPI imaging over time. Quantitative analysis revealed a 41% decrease in Fe content at the tumor site by day 26, correlating with the absence of bioluminescence signals and indicating effective cancer cell death.

In recent years, patient-derived xenograft (PDX) models have gained increasing attention as superior alternatives to conventional cancer cell lines, as they more accurately capture the complex heterogeneity of human tumors. As a result, findings derived from PDX studies tend to have greater clinical relevance. Developing strategies that enable high-quality imaging and real-time monitoring of PDX growth and behavior in living systems is therefore of significant interest. Knier and colleagues introduced the first effective approach for iron-labeling PDX cells, marking a milestone as it also represented the initial successful iron-labeling of breast cancer cells obtained from patient brain

 doi:10.20944/preprints202509.0352.v1

metastases [76]. By combining bioluminescence imaging to assess cell viability with MPI for the detection and quantification of SPIONs, they demonstrated highly sensitive, longitudinal tracking of pre-labeled F2–7 PDX cells using micron-sized iron oxide particles. The resulting MPI signals provided insights into both tumor cell viability and proliferation over time.

In a separate effort aimed at advancing imaging technologies for tracking primary and metastatic cancer sites, Parkins et al. leveraged the phenomenon of tumor self-homing [76]. This refers to the ability of CTCs, shed from the primary tumor into the bloodstream, to preferentially migrate back and colonize existing tumors rather than healthy tissues, thereby promoting metastatic progression. Their study was the first to show that MPI could sensitively detect systemically delivered SPION-labeled CTCs and visualize their homing behavior. Conducted in a mouse model with pre-established human breast cancer lesions, the labeling process did not impair cell viability. The work offered valuable insights into unintended tumor targeting, as well as the dynamics of CTC infiltration, proliferation, survival, and the potential biological mechanisms underlying the self-homing process.

5.1.2. Immune Cell Tracking

Immune cell tracking helps to understand cancer progression at the tumor microenvironment (TME) in terms of initialization, growth and metastasis. The rapid advancements in cancer immunotherapy have created an urgent need for imaging techniques that can systematically monitor immune cell distribution and dynamics within the tumor microenvironment (TME) over time and assess therapeutic efficacy. Conventional approaches such as SPION-based ^{1}H MRI and ^{19}F MRI have been employed for immune cell tracking; however, these modalities often fall short in sensitivity and long-term monitoring capabilities. In contrast, MPI offers a powerful alternative by enabling the in vivo tracking of SPION-labeled immune cells throughout the entire lifespan of the tagged cells, addressing key limitations of traditional methods [77].

Earlier approaches using cellular MRI have relied on the passive uptake of SPIONs by tumor-associated macrophages (TAMs) to indirectly visualize their distribution within tumors [78,79]. Building on this concept, Makela and colleagues were the first to apply MPI for real-time tracking and detection of SPION-labeled TAMs delivered intravenously in a mouse model of 4T1 breast cancer [80]. This method enabled precise quantification of iron-labeled macrophages and their migration into tumors, outperforming comparable MRI-based assessments. In a related study, Gerosa et al. demonstrated that MPI could detect TAMs labeled directly within the tumor at very low doses of Synomag-D (approximately 3 mg/kg) [81]. Further advancing this field, Mansfield and collaborators explored the use of MPI to monitor TAM responses to an anti-CD47 monoclonal antibody therapy [82]. CD47 is a membrane protein frequently overexpressed by cancer cells, allowing them to evade immune recognition. By blocking CD47 with therapeutic antibodies, macrophage-mediated phagocytosis of cancer cells can be restored. MPI scans taken at 1, 3, and 7 days after tracer administration revealed progressively stronger signals at the tumor site in treated animals compared to controls, indicating enhanced TAM accumulation and suggesting improved therapeutic efficacy.

MPI has emerged as an effective non-invasive technique for monitoring adoptive cellular therapy (ACT) T cells within living subjects, as demonstrated in preclinical brain tumor models by Rivera-Rodriguez and colleagues. This approach supports the advancement of improved ACT strategies for various malignancies [83]. T cells can be labeled outside the body using clinically available magnetic resonance tracers such as ferucarbotran, without negatively affecting their viability, phenotype, or cytotoxic activity under studied conditions. Microscopic analysis has confirmed the presence of ferucarbotran nanoparticles inside T cells and their association with the cell membrane. MPI offers precise quantification of labeled T cells, showing a strong linear relationship between signal intensity and cell number (approximately 1 pg Fe per cell). In vivo experiments have revealed that MPI can track ferucarbotran-labeled T cells, map their biodistribution to sites like the lungs, liver, and tumors, and demonstrate signal overlap with fluorescence from

 doi:10.20944/preprints202509.0352.v1

genetically engineered T cells, verifying that the detected MPI signal originates from living labeled cells.

Magnetic Particle Imaging has also been explored for tracking various immune cell types beyond T cells, including macrophages, dendritic cells, B cells, and natural killer (NK) cells [82]. Studies examining macrophage trafficking have revealed their predominant accumulation at the invasive edges of tumors in tumor-bearing mice, while in healthy mice their distribution differs. Moreover, MPI enables highly sensitive monitoring of dendritic cell migration, with detection thresholds reaching roughly 4,000 cells in live animal models and about 2,000 cells in ex vivo assessments [84].

5.1.3. Imaging and Tracking Inflammatory Cells

Tumors involve not only cancer cells but also immune-mediated inflammation, which drives tissue response to damage and irritants. Monitoring localized inflammation can aid disease diagnosis and therapy evaluation. Characterized by vasodilation, fluid accumulation, and immune cell recruitment, inflammation has traditionally been tracked using invasive methods or low-specificity imaging. While SPION-enhanced MRI has enabled detection of inflammatory activity [85,86], MPI offers superior sensitivity and specificity [87,88]. Inflammation can be monitored by labeling phagocytic cells ex vivo or by direct nanoparticle injection for in situ uptake, allowing precise tracking of immune cell migration and accumulation at inflamed sites. Remmo et al. show cased the utility of tracking THP-1 monocytes using two different tracers Syn-COOH and SynD-PEG, using MPI [89]. Syn-COOH with citrate coating possess an average hydrodynamic diameter of 23.4 ± 6.2, whereas as SynD-PEG with PEG–dextran coating showed an average size of 47.7 ± 17.2 nm. Studies showed that Syn-COOH showed a larger cell uptake than SynD-PEG in two different media such as PBS and RPMI allowed a MPI based detection of 1.1 pg/cell.

Mangarova and colleagues explored the use of MPI to monitor vascular inflammation in abdominal aortic aneurysms (AAAs) outside the living organism [90]. AAAs, characterized by the weakening and enlargement of the abdominal aorta commonly in its infrarenal segment are a significant cause of mortality in developed nations. In their study, the team evaluated inflammatory activity within the aneurysmal walls of Angiotensin II-treated ApoE−/− mice using a combination of in vivo MRI, ex vivo MPI, and ex vivo magnetic particle spectroscopy (MPS). Ex vivo MPI scans were conducted 24 hours after intravenous injection of ferucarbotran (Resovist), following a 3–4-week Angiotensin II treatment regimen. The findings showed a substantial accumulation of iron in the aneurysmal regions, taken up by macrophages, highlighting the capability of ex vivo MPI to sensitively detect vascular inflammation. These observations were closely aligned with ex vivo MPS measurements, confirming both the presence of inflammation and the associated deposition of iron nanoparticles in the aneurysmal tissue.

Non-invasive visualization of white blood cell (WBC) migration offers a promising strategy for monitoring and diagnosing inflammatory conditions. Conventional approaches often rely on direct radionuclide labeling of WBCs for scintigraphy or SPECT imaging; however, these methods are limited by high costs, radiation exposure, and the need for large tracer doses, making them impractical for routine screening. In a recent study, Chandrasekharan et al. introduced MPI as a sensitive, radiation-free alternative for tracking WBCs at inflammation and infection sites [88]. The study employed commercially available multi-core anti-Ly6G SPIONs (Miltenyi Biotec GmbH) conjugated to antibodies, which selectively bind to the Ly6G antigen on neutrophils. Prior to animal studies, the MPI performance of these nanoparticles was characterized, revealing enhanced spatial resolution (1.26 mm) and approximately 1.8-fold higher sensitivity compared to multi-core VivoTrax. In vivo experiments were conducted in a murine model of lipopolysaccharide-induced myositis, with nanoparticles administered intravenously after inflammation induction. MPI successfully visualized the targeted accumulation of WBCs at inflamed tissue sites, yielding strong contrast-to-noise ratios between 8 and 13, demonstrating precise and sensitive detection of inflammatory regions.

 doi:10.20944/preprints202509.0352.v1

5.2. In Vivo Tumor Imaging

Solid tumors undergo accelerated logarithmic growth around 10^5 cells, triggered by an angiogenic switch, as described by the Gompertzian model [91]. Early cancer detection is crucial for better outcomes, and MPI offers promise due to its sub-micromolar sensitivity and radiation-free imaging. Preclinical studies show that SPIONs accumulate in tumors through three main routes: passive diffusion via leaky vasculature and poor lymphatic drainage (EPR effect), ligand-mediated targeting [83,92];] and magnetic field-guided delivery [93]. The latter two mechanisms represent active targeting strategies, which are particularly relevant for MPI-based imaging.

MPI was first applied to cancer research to visualize passive nanoparticle accumulation and the EPR effect in living systems. In this study, Yu et al. developed long-circulating SPIONs (LS-008) and delivered them intravenously into tumor-bearing rats (Figure 6A,B) [94]. Due to MPI's high intrinsic sensitivity, signal-to-noise ratios reached up to 50 (Figure 6C). The nanoparticles initially localized along the tumor margins, reaching maximum accumulation around six hours post-injection, followed by gradual clearance beyond 48 hours as studied by bioluminescence and MPI/CT (Figure 6D,E). This pioneering work highlighted the potential of MPI for innovative cancer imaging strategies. Subsequent research has further refined nanoparticle designs for MPI. For instance, Janus particles have enabled the labeling of cancer cells and allowed detection of as few as 250 cells in vivo [14]. Moreover, fluorescent Janus-based MPI probes have supported multimodal imaging and cell tracking, while other hybrid tracers, such as FeCo@C PEG and TB/SPIO@PS-PEG (TSP) nanoparticles, have shown promise for enhancing imaging signals, enabling hyperthermia therapy, and facilitating long-term tumor monitoring [60,95].

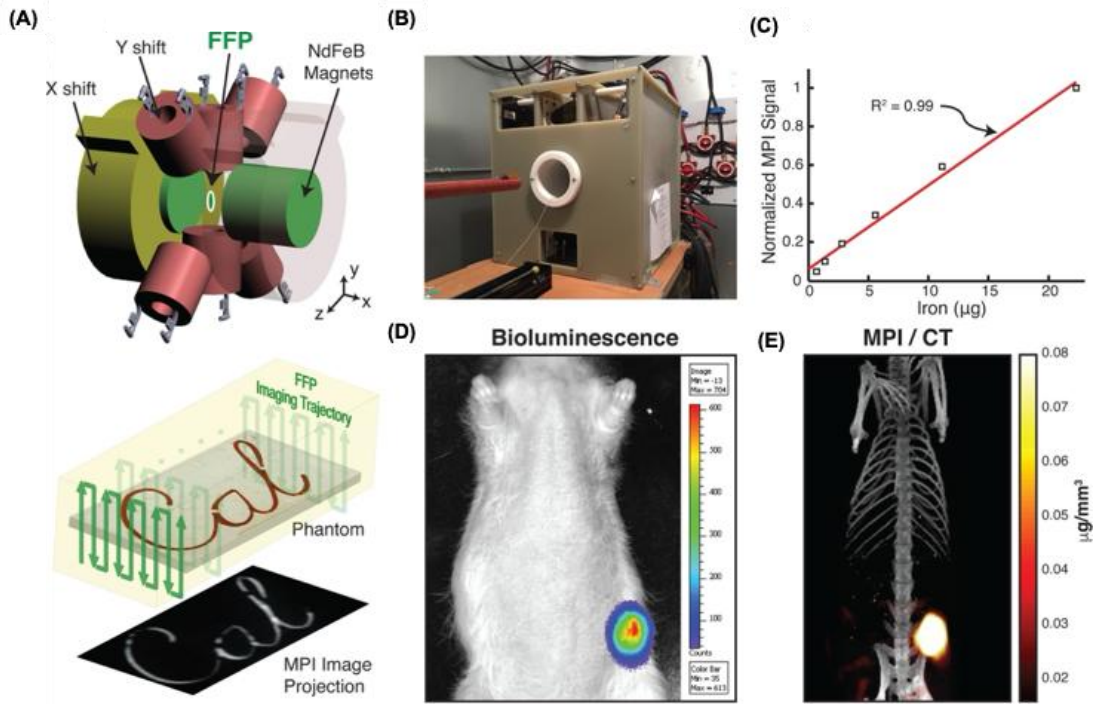

Figure 6. In vivo tumor imaging applications (A) Schematic representation of field-free point (FFP) magnetic particle imaging. A magnetic field gradient is generated using NdFeB permanent magnets (green), while electromagnets (yellow and red) shift the FFP along the x- and y-axes. Motion of the animal bed along the z-axis is controlled by a motor, enabling the FFP to traverse the sample within the field of view and produce a 3D MPI dataset. A maximum intensity projection of the reconstructed 3D image is displayed. (B) Photograph of the custom-designed FFP MPI scanner. (C) Quantitative MPI response of LS-008 superparamagnetic iron oxide (SPIO) nanoparticles (Lodespin Labs) at concentrations from 36 µg Fe/mL to 1.2 mg Fe/mL, demonstrating a linear correlation between SPIO concentration and MPI signal ($R^2 = 0.99$). (D) Bioluminescence image of an MDA-MB-231-luc xenograft tumor. (E) Corresponding maximum intensity projection of the MPI scan (field of view: 4

 doi:10.20944/preprints202509.0352.v1

× 4 × 5.8 cm) acquired 6 h after intravenous injection of LS-008 particles, shown with CT overlay of the lower abdomen. Reproduced with permission from [94], 2017, American Chemical Society.

Arami et al. demonstrated that MPI with functioned SPIONs, namely lactoferrin-conjugated SPIONs, had high sensitivity with which to detect 1.1 ng of iron (SNR of ~3.9) at a spatial resolution of approximately 600 μm [92]. MPI based approaches have shown promise for both imaging and therapy. You et al. developed propranolol-loaded SPIONs that enabled highly sensitive and specific visualization of prostate cancer nerve density via MRI and MPI, while also improving survival and reducing nerve proliferation markers [96]. Circulating tumor cells, which naturally home to tumor sites, have also been explored as therapeutic carriers. Using micro-sized iron oxide particles with high iron payloads, Parkins et al. demonstrated successful tracking of labeled circulating tumor cells to breast tumors, illustrating MPI's potential for targeted cell-tracking applications [76].

Recent advancement in MPI allowed for the detection of breast cancer with various passive and actively targeting SPIONS. A novel handheld, human-scale MPI device has been developed for precise sentinel lymph node (SLN) detection in breast cancer [97]. The system integrates a highly sensitive MPI probe, concentric coils for spatial encoding, and a solenoid coil for uniform excitation, while mirrored coils suppress noise by up to 100 dB. In preclinical rat studies, it successfully detected 54 μg of SPIO tracer (≈1.2% of total injected iron) in SLNs, with an optimal detection window of 4–6 minutes post-injection. Yang et al. developed an iron oxide nanoprobe conjugated with indocyanine green and hyaluronan for targeted breast cancer imaging [98]. Exploiting the overexpression of CD44, the primary hyaluronan receptor on most breast cancer cells, this probe enabled dual-modality detection of primary tumors and lung metastases in a transgenic mouse model using both MPI and NIR fluorescence imaging. This work represents the first use of HA-based nanoparticles for MPI, offering a promising platform for noninvasive breast cancer and metastasis detection.

Kumar et al. fabricated iron oxide nanochains (FeONCs) with an average core diameter of 17.4 nm as a MPI tracer for addressing the current limitations terms of sensitivity and resolution [50]. Superconducting Quantum Interference Device magnetometry measurements confirmed the superparamagnetic nature of FeONCs, a prerequisite for MPI tracers, with a saturation magnetization of 144.34 emu/g, significantly higher than FeONPs (33.56 emu/g) and FeO nanocubes (68.28 emu/g). This increased magnetic moment enhances their ability to respond quickly and effectively to magnetic fields, making them ideal for MPI. Magnetic relaxometry studies indicated that FeONCs provided significantly higher signal intensity than commercially available tracers like VivoTrax (4.3 times higher), Synomag-D-70 (2.03 times higher), and Synomag-D50 (1.56 times higher). Cell viability studies using 4T1 breast cancer cells and mesenchymal stem cells showed no toxicity at concentrations up to 100 μg/mL of FeONCs with DSPE-PEG and RGD on their surfaces. In vivo experiments using orthotopic breast cancer mouse models demonstrated that RGD-based FeONCs accumulated in the tumor region earlier and with enhanced MPI signals compared to non-RGD and control spherical FeONPs and a clear anatomical feature co registered with CT allow early detection and tracking of breast cancer.

5.3. Theranostic Applications

The capability of MPI using SPIONS for imaging and use the therapeutic properties of SPIONS such as drug delivery, and magnetic fluid hyperthermia come up with new inventions for tumor studies.

5.3.1. Drug Delivery Tracking

Stimuli responsive drug carriers are quite interesting these days, since such smart materials can show controlled release of drugs at specific site and can increase the drug delivery at specific location. Zhu et al. designed the first 'smart' activatable probe for MPI drug delivery applications [69]. They have prepared a SPION cluster loaded with Doxorubicin (DOX) and coated it with poly(lactic acid) polymer, which can degrade in acidic environment at pH 6.5, and can simultaneously release DOX

 doi:10.20944/preprints202509.0352.v1

at tumor site (Figure 7A). Owing to this the MPI response for the SPIONS increase due to the recovery of Brownian relaxation. MPI signal quantification give a measure of DOX release, and this allows accurate quantitation and monitoring of drug release in vitro and in vivo (Figure 7B,C). Fuller et al. developed multifunctional magnetic nanocarriers that co-encapsulate DOX and SPIONs within a hydrophobic core and are coated with PEG–poly(lactic acid) for solubility and stability (Figure 7D) [99]. Their drug and SPION release is pH-responsive, enabling controlled delivery of DOX and it was confirmed by MPI signal intensity (Figure 7E). Similarly, Tomitaka et al. designed NIR-responsive nanostars with a SPION core and plasmonic gold shell; attached drugs are released via photothermal activation and monitored in real time using MPI [100].

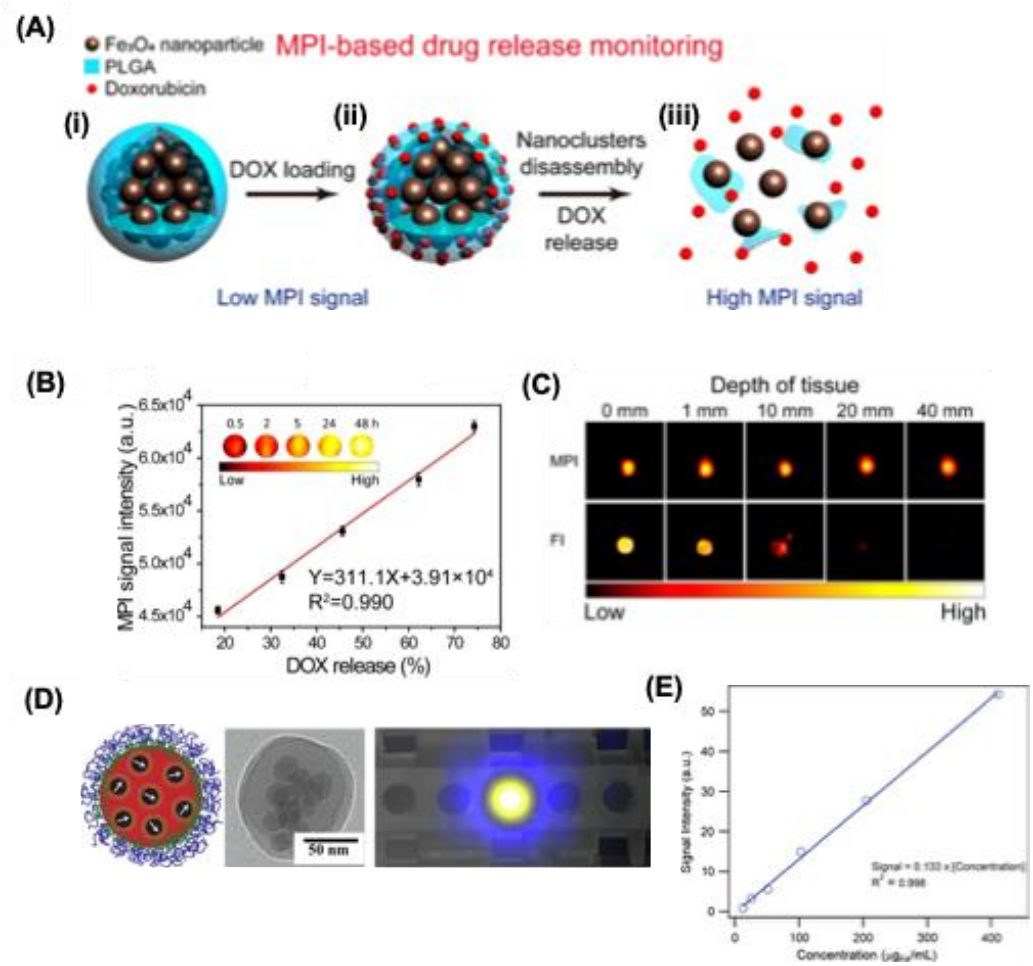

Figure 7. Drug delivery applications. (A) Schematic of Fe_3O_4@PLGA nanocomposites for MPI-guided drug release. (i) Fe_3O_4 nanoparticles (brown) encapsulated in a PLGA shell (blue) are loaded with DOX (red). (ii) In acidic conditions, the PLGA degrades, leading to DOX release and Fe_3O_4 core disassembly. (iii) Core clustering reduces MPI signal, while gradual disassembly enhances it, enabling quantitative monitoring of drug release. (B) Relationship between the percentage of DOX released and corresponding MPI signal intensity. A strong linear correlation was observed, with R^2 = 0.99. Inset: Representative MPI scans of samples incubated in phosphate buffer (pH 6.5) at varying time intervals, displayed using pseudocolor mapping. (C) Depth penetration comparison of MPI and fluorescence using Cy5.5. conjugated SPIONS loaded with Cy5.5 were placed in a 96-well plate and sequentially covered with chicken breast tissues of varying thickness. MPI and FI measurements were performed at each depth, with corresponding signal intensities displayed in pseudocolor. (D) Schematic and representation for the SPIONS loaded with DOX, and TEM images showing the protective PEG layer loaded with SPION-DOX. MPI images for the SPIONS loaded with DOX. (E) Quantitative MPI analysis of doxorubicin-loaded nanocarriers. Reproduced with permission from [69], 2019, American Chemical Society and from [99], 2019, Elsevier publishing group.

 doi:10.20944/preprints202509.0352.v1

Extracellular vesicle (EVs) known to pass blood brain barrier easily and exploited to deliver therapeutic agents to brain metastases. To advance this area of research, it is crucial to gain insights into the behavior, distribution, and build-up of EVs during metastasis. Toomajian and colleagues investigated this by tracking SPION-labeled EVs in brain metastases using MPI [101]. In their in vivo study, mice were first administered intracardiac injections of 4T1-BR Fluc/GFP breast cancer cells, which form brain metastases and express firefly luciferase to enable bioluminescence imaging (BLI). The SPION-tagged 4T1 EVs were then introduced either at early or advanced stages of metastatic development and monitored through MPI and BLI to assess when EVs localized to metastatic regions. The results demonstrated that EVs can penetrate the blood–brain barrier and accumulate at tumor sites, highlighting their promise for therapeutic applications. Furthermore, the study underscores MPI's potential for real-time monitoring of treatment efficacy.

Exosomes are nanoscale extracellular vesicles (30–200 nm) long studied as drug carriers but only recently visualized using MPI [102]. Jung et al. first demonstrated in vivo MPI tracking of exosomes derived from MDA-MB-231 breast cancer cells labeled with SPIONs and Olaparib, a PARP inhibitor used in cancer therapy [103]. This strategy enables simultaneous imaging and targeted delivery to hypoxic tumor regions, addressing a key challenge in treatment resistance and underscoring the theranostic potential of MPI-labeled exosomes.

5.3.2. Magnetic Fluid Hyperthermia

Magnetic fluid hyperthermia (MFH) involves administering magnetic nanoparticles locally or systemically and applying an alternating magnetic field (AMF) to heat areas of particle accumulation [104]. Heat arises from rapid SPION magnetisation and Brownian relaxation, damaging nearby tissue. Two main therapeutic strategies exist: (i) mild hyperthermia, maintaining ~42 °C to trigger cancer cell apoptosis with minimal harm to healthy tissue, and (ii) ablation, causing necrosis at >46 °C but risking collateral damage. The treatment's efficiency is measured by the specific absorption rate (SAR), i.e., magnetic power absorbed per nanoparticle mass. Though first proposed in 1957, MFH remains actively studied due to benefits such as unlimited tissue penetration, compatibility with other therapies, and internalised heat delivery. Applications include whole-body MFH, where AMF coils scan the body, and local MFH, where surface coils target shallow lesions. Key challenges include poor nanoparticle localisation and off-target heating in organs like the liver and spleen, leading to toxicity. To address this, researchers developed MPI–MFH, combining MFH with MPI [105]. MPI provides quantitative maps of SPION distribution, enabling precise SAR prediction and spatially confined heating to the field-free region (FFR). By adjusting gradient strengths, the FFR can be tuned to lesion size, enabling high-resolution, depth-independent targeting while reducing off-target effects. This integrated approach offers a pathway for safer and more effective clinical translation.

MPI and MFH share similar physics, enabling the same SPIONs and allowing integration into a single device that switches between imaging and heating by adjusting the AC field. Hensley et al. developed the first combined MPI–MFH system, achieving selective heating of 3 mm-separated phantom targets with SAR up to 150 W g^{-1} and heating rates of 0.4 °C s^{-1} [105]. Tay et al. later applied this system in vivo, localizing thermal dose in dual-tumor mice with 7 mm spatio-thermal resolution, minimal off-target toxicity, and a six-fold tumor activity reduction (Figure 8A) [18]. Higher resolution (~2.3 mm) is theoretically possible with stronger magnetic gradients (7 T m^{-1}). They sequentially applied heat to various in vivo sites while avoiding the unintended tumor regions. The thermal dosage was evaluated using MPI signal intensity (Figure 8B,C). This combined MPI–MFH system offers a promising approach for image-guided therapy, precise spatial targeting, and optimized thermal dose planning.

Recent advancements have led to the development of commercial MPI–MFH platforms, such as the HYPER system by Magnetic Insight (0.5–2.6 T m^{-1} gradient, 340 kHz, 15 mT) Significant efforts have also focused on engineering SPIONs optimized for imaging and hyperthermia, emphasizing colloidal stability, narrow size distribution, and strong magnetic properties. Using a micromixer platform, Bleul et al. synthesized monodisperse single-core SPIONs (~30 nm) that delivered high MPI

 doi:10.20944/preprints202509.0352.v1

signals and exceptional SAR values (>1 kW g(Fe)$^{-1}$), outperforming Resovist threefold [106]. Similarly, Du et al. created single-core SPIONs with enhanced therapeutic heating [107]. Functionalizing these particles with CREKA peptides, which bind fibrin–fibronectin complexes overexpressed in tumors, further improved delivery and cancer ablation efficiency.

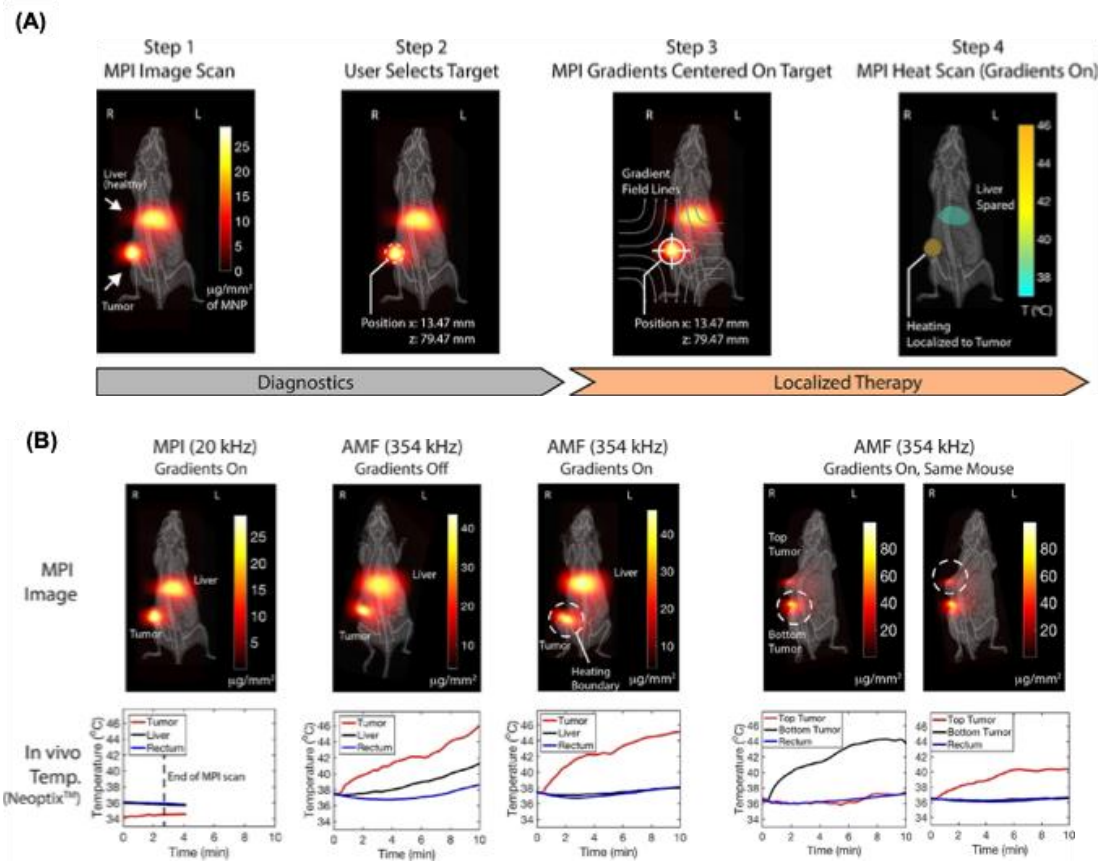

Figure 8. MPI hyperthermia application. (A) Theranostic workflow in a U87MG xenograft mouse using SPIONs. (Step1) MPI scan at 20 kHz, 20 mT shows SPION distribution in tumor and liver without heating. (Step 2) Tumor is selected as the target for localized hyperthermia. (Step 3) MPI gradients shift the field-free region (FFR) to the tumor, saturating SPIONs elsewhere. (Step 4) Heat scan at 354 kHz, 13 mT with MPI gradients on generates localized tumor heating while sparing the liver. (B-C) In vivo demonstration of targeted magnetic hyperthermia with MPI and the heating trajectory represents the heating process. The heating effect was confined to the tumor, with minimal impact on the liver. Local temperatures in the mouse were recorded using Neoptix fiber optic sensors. Under a standard MPI scan at low frequency (20 kHz) with a raster scan trajectory, negligible heating was detected throughout the animal. Reproduced with permission from [18], 2018, American Chemical Society.

One key aspect influencing the heating efficiency of SPIONs is the nature of their surface coating. Jordan and colleagues were the first to report differences in specific absorption rate (SAR) between dextran-coated and aminosilane-coated particles, with the latter showing about a 1.2-fold higher SAR under comparable conditions [108]. Liu and co-workers later conducted a systematic study examining SPIONs coated with polyethylene glycol of varying molecular weights, finding that thinner coatings led to improved SAR [109]. This enhancement is primarily linked to Brownian relaxation-driven heat dissipation; however, excessively reducing the coating thickness can compromise the colloidal stability of the nanoparticles, thereby negatively affecting SAR. Beyond coatings, particle shape also plays a significant role. Khurshid et al. demonstrated that cubic SPIONs exhibit roughly a 1.4-fold increase in SAR compared to spherical ones [110]. Bauer et al. further confirmed the superior performance of cubic SPIONs, particularly when selectively doped with

 doi:10.20944/preprints202509.0352.v1

anisotropic zinc [64]. Their work revealed a twofold increase in MPI signal and a fivefold enhancement in SAR relative to undoped single-core spherical SPIONs.

5.3.3. Navigation for Intraoperative

Achieving complete surgical removal of a tumor is critical to minimize the chances of recurrence. Therefore, there is a strong need for imaging strategies that can accurately assess tumor margins and identify metastatic lymph nodes during surgery. Existing methods for margin visualization offer high sensitivity and specificity [111]. Nevertheless, no single technique has yet provided a comprehensive solution, as current approaches often yield false positives, require lengthy analysis, depend heavily on specialized expertise, and face limitations in tissue penetration depth [9]. MPI is being developed for real-time margin assessment in breast-conserving surgery to reduce re-excisions caused by positive margins (Figure 9A). It employs tumor-targeted iron oxide agents and two devices: a hand-held detector to identify residual tumor at the incision site and a small-bore scanner to rapidly image excised specimens [111]. Proof-of-concept studies show detection of as little as 100 ng of iron oxide (~790 μm tumor) and rapid 10.7 s scans of 3D lumpectomy phantoms, enabling precise tumor localization and margin evaluation (Figure 9B). This intraoperative strategy could improve complete tumor removal and increase negative-margin rates. Azargoshasb et al. explored the use of freehand MPI integrated with fluorescence guidance to achieve three-dimensional virtual mapping of sentinel lymph nodes. Their findings indicate that combining freehand MPI with either SPIONs alone or a mixture of SPIONs and indocyanine green could potentially serve as an alternative to intraoperative frozen tissue biopsy in phantom models, ex vivo human skin samples, and live porcine surgeries [112].

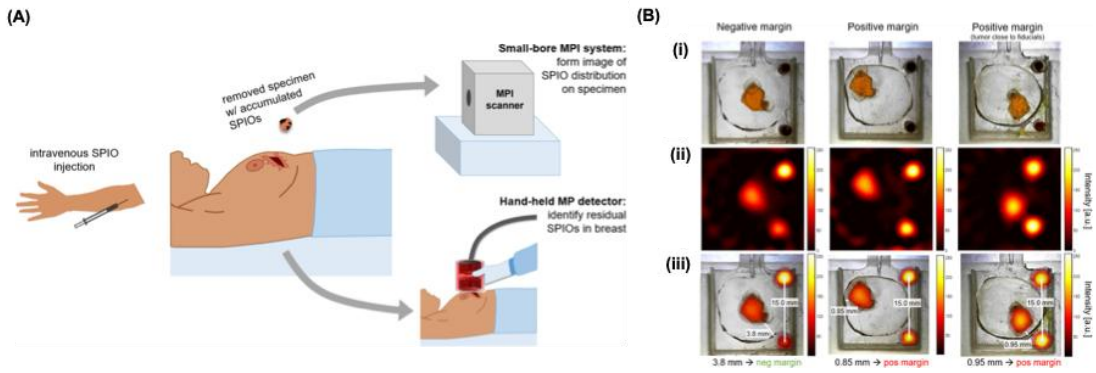

Figure 9. Intraoperative application using MPI. (A) MPI workflow for breast-conserving surgery. SPIOs are injected intravenously and allowed to accumulate in the tumor while clearing from the vasculature. After tumor excision, the specimen is imaged in a small-bore MPI scanner, and a hand-held detector identifies residual SPIOs at the surgical site, indicating remaining tumor. Figure created with MS PowerPoint. (B) Lumpectomy phantom imaging and MPI co-registration. (i) Optical views of lumpectomy phantoms. Tumors are 6.5 mm cavities filled with 0.5 mg/mL VivoTrax (51.2 μg Fe), and fiducials are 1.75 mm cylinders with undiluted 5.5 mg/mL VivoTrax (61.1 μg Fe). Healthy tissue consists of SPIO-free 3D-printed material. Negative margins correspond to tumor >1 mm from the surface; positive margins are ≤1 mm. (ii) MPI images were acquired in 10.7 s using a triangular-waveform shift with 27 projections, 66 readouts per projection, and 150 Tx cycles per readout. Data were reconstructed via model-based preconditioned conjugate gradient, scaled to each image's maximum. (iii) Co-registration of MPI and optical images was performed using fiducials. Tumor-to-margin distances were measured in MATLAB, accurately distinguishing negative and positive margin phantoms. Reproduced with permission from [111], 2021, Nature publishers.

 doi:10.20944/preprints202509.0352.v1

5.3.4. Combinatorial Therapies

Theranostic platforms can be adapted for combination therapies, enabling on-demand drug release from nanocarriers alongside hyperthermia with precise spatial temporal control. Drug liberation is tunable by adjusting the AMF strength and remains minimal without AMF exposure [113]. Maruyama et al. reported thermosensitive liposomes co-encapsulating SPIONs and doxorubicin, demonstrating MPI-based monitoring of release triggered by AMF-induced membrane disruption [114]. Their prototype scanner (400 Hz, 16 mT) operates at higher drive amplitudes and lower frequencies than most commercial systems, affecting resolution and signal strength. Rost et al. later confirmed comparable MPI performance of SPION-loaded liposomes on the commercial MOMENTUM scanner (45 kHz, 16 mT) [115]. Similarly, Fuller et al. developed a drug–polymer conjugate containing ~18 nm semispherical SPIONs, showing spatially controlled release via thermal cleavage of a Diels–Alder bond [116]. The release can be repeatedly activated and monitored with MPI, while magnetic field gradients localize therapy and limit off-target effects.

6. Machine Learning Assisted MPI

Machine learning (ML) techniques, especially, K-means clustering and deep learning (DL) approaches, are increasingly crucial for advancing MPI. These methods address key challenges in MPI, including image segmentation, quantitative analysis, reconstruction, and faster calibration, thereby enhancing both image quality and efficiency [117]. Incorporating ML into MPI also broadens its potential clinical and research applications. For instance, Hayat et al. applied the K-means algorithm, a standard unsupervised ML tool, to segment regions of interest in MPI images and quantify iron content. This approach has been successfully utilized across in vitro, in vivo, and ex vivo datasets [118]. Similarly, Sun et al. demonstrated that K-means-based ML analysis can track islet organoid grafts labeled with SPIONs, offering a consistent and reproducible framework for MPI image segmentation and quantitative assessment [119].

Recent progress in MPI has been propelled by innovative image reconstruction strategies that utilize deep learning (DL). One promising approach involves deep image priors, which employ neural networks to model the reconstruction solution directly. When compared with conventional variational and iterative regularization methods, this technique demonstrates marked improvements in peak signal-to-noise ratios (SNR) and structural similarity metrics. Such developments underscore the potential of machine learning to produce high-fidelity reconstructions, a critical factor for advancing MPI in clinical settings [120].

Given the lack of MPI datasets aligned with ground truth and the variability inherent to particle-based imaging, incorporating regularization terms into reconstruction networks has emerged as an effective way to reduce dependency on large training datasets. Deep unfolding methods exemplify this strategy by embedding optimization steps directly into DL layers, contrasting with standard CNN training. The deep equilibrium (DEQ)-MPI framework highlights how unfolding-based optimization can further enhance reconstruction quality. Additionally, the rise of untrained neural networks has generated new opportunities in MPI reconstruction, enabling methods such as Deep Image Prior (DIP) and deep plug-and-play (PP)-MPI to reconstruct images without predefined network inputs [121]. Machine learning in MPI also enhances spatial resolution and system matrix calibration, both critical for imaging performance. Traditional methods to improve resolution often come with higher costs, reduced sensitivity, or lower contrast. To address this, ML approaches have been developed: for instance, Dittmer et al. used deep learning to generate high-resolution images from low-resolution inputs [122], while Güngör et al. employed a CNN with residual-dense blocks to refine the system matrix and achieve more accurate reconstructions [123]. Overall, integrating ML into MPI holds promise for advancing preclinical applications of emerging medical imaging techniques.

7. Clinical Translation

 doi:10.20944/preprints202509.0352.v1

Commercial preclinical MPI scanners are currently limited to Magnetic Insight Inc. and Bruker GmbH. Over the past decade, advances in software and reconstruction algorithms have significantly improved their performance. For instance, hybrid system matrices have been shown to reduce calibration time by up to 50% while enhancing spatial resolution and quantitative accuracy. Some state-of-the-art small-animal MPI systems now achieve resolutions on the order of 0.5–1.0 mm and detect SPION concentrations as low as a few nanograms of iron per milliliter, highlighting their sub-micromolar sensitivity.

Scaling MPI to clinical applications presents unique challenges. Beyond the ergonomic and engineering hurdles of human-scale magnets, there are concerns over potential allergic reactions to SPION formulations and the high-power demands needed to achieve sufficient magnetic field amplitudes. For example, clinical-scale scanners may require drive field amplitudes of 5–10 mT and gradients exceeding 5 T/m, which dramatically increase cost and energy consumption. Early apprehensions about tissue heating and peripheral nerve stimulation have been mitigated by studies demonstrating that optimized drive frequencies (below ~150 kHz) and amplitudes can remain within safe biological thresholds without sacrificing imaging quality.

Several promising clinical-scale prototypes illustrate MPI's potential impact. Graeser et al. developed a brain-dedicated MPI system that operates with lower technical requirements and allows rapid, flexible imaging for potential stroke or tumor diagnostics. Similarly, Mason and colleagues designed a small-bore 2D field-free-line (FFL) MPI projection imager capable of mapping intravenously delivered SPIONs in excised breast tissue during surgery. This system enables real-time tumor margin assessment, potentially reducing the high re-excision rates seen in breast-conserving surgery.

A critical bottleneck remains the lack of clinically approved SPIONs optimized for MPI. Conventional MRI agents are suboptimal for MPI physics, but tailored nanoparticle designs have already demonstrated substantial improvements. For example, monodisperse iron oxide cores of ~20–30 nm with optimized magnetic anisotropy have achieved superior signal intensity and sharper point-spread functions. Fine-tuning SPION size, coating (e.g., PEG, dextran), and surface charge can improve biodistribution and reduce clearance by the reticuloendothelial system. Furthermore, MPI resolution can be enhanced with optimized SPIONs, allowing lower magnetic gradients (<2 T/m), thereby reducing the technical burden of large-scale systems.

Emerging research focuses on multifunctional and activatable nanomaterials. Smart SPION assemblies are being explored that carry drugs or targeting ligands and release payloads in response to environmental triggers such as pH, enzymatic activity, or near-infrared (NIR) light. For example, enzyme-responsive SPION clusters have been proposed for in vivo detection of matrix metalloproteinase activity, while plasmonic-gold-coated SPIONs can achieve NIR-triggered drug release with simultaneous MPI tracking. These advances suggest a future where MPI could not only image but also provide real-time functional and therapeutic monitoring. Overall, the integration of optimized SPIONs with advanced hardware design and safety strategies is expected to accelerate MPI's clinical translation, particularly for brain imaging, intraoperative cancer margin assessment, and early-stage disease screening.

8. Conclusions and Perspective

Magnetic Particle Imaging (MPI) has emerged as a cutting-edge, radiation-free imaging modality that utilizes superparamagnetic iron oxide nanoparticles (SPIONs) as tracers. Its fundamental advantages include unparalleled depth-independent sensitivity, minimal background signal, and a strictly linear relationship between signal intensity and nanoparticle concentration. This enables precise quantification of SPION distribution even in anatomically difficult regions such as lung tissue, bone marrow, or other organs with complex structures. Such features allow MPI to achieve nearly infinite contrast with extremely low detection limits, making it ideal for applications that demand both accuracy and safety. Over the last decade, MPI has demonstrated significant promise in preclinical studies for diverse biomedical uses, including image-guided magnetic fluid

 doi:10.20944/preprints202509.0352.v1

hyperthermia, targeted drug delivery, inflammation mapping, perfusion analysis, and tracking of therapeutic or immune cells in vivo.

The progression of MPI toward clinical translation, however, depends heavily on optimizing nanoparticle design and improving system-level performance. Researchers are focusing on tuning critical physicochemical parameters such as particle core size and shape, surface coatings, and magnetic relaxation properties. Determining whether single- or multi-core structures are more appropriate for specific clinical goals is an area of active investigation. Despite these advances, challenges persist; nanoparticles often exhibit heterogeneous accumulation within tumors and passive uptake by the reticuloendothelial system in the liver and spleen, which can reduce targeting specificity. Furthermore, reports of reactive oxygen species generation and potential neurotoxicity highlight the need for comprehensive safety assessments and the development of safer or stimulus-responsive tracers.

To overcome these hurdles, several strategies are being explored. Multi-color MPI techniques, which enable the simultaneous imaging of multiple tracers or physiological parameters, may facilitate real-time therapy monitoring, such as during hyperthermia, by providing direct feedback on local heating. Innovations in imaging sequences, nanoparticle engineering, and gradient field design could improve resolution to sub-millimeter scales, greatly enhancing diagnostic detail. Parallel advances in hybrid systems that integrate MPI with complementary modalities like MRI or CT offer anatomical context to the molecular specificity of MPI. Furthermore, portable and bedside MPI scanners are being developed for critical care or emergency settings, where rapid, repeated, and non-ionizing imaging would be particularly valuable.

Beyond oncology, MPI's future potential spans numerous therapeutic and diagnostic domains. It could enable real-time 3D imaging for gastrointestinal and biliary disorders while minimizing radiation exposure, and inhalable SPION-based aerosols may one day allow for targeted treatment and monitoring of respiratory conditions like asthma. Immune-targeted tracers could help evaluate patient response to immunotherapies dynamically. Importantly, integrating diagnosis, therapeutic targeting, and treatment feedback within a single MPI platform represents one of the most transformative opportunities in biomedical imaging. While hardware challenges remain—including the need for stronger magnetic field gradients, larger bore sizes, improved cooling systems, and cost-effective scalability continued advances in both instrument design and nanoparticle chemistry suggest that MPI is poised to become a powerful clinical tool for precision medicine.

Funding: No funding obtained for this review article

Acknowledgments: P.P.P.K. shows sincere gratitude to the Department of Biomedical Engineering, Michigan State university, for the facilities and use of resources for the literature collections.

Conflicts of Interest: The author declares no conflict of interest.

References

1. Hussain, S.; Mubeen, I.; Ullah, N.; Shah, S.S.U.D.; Khan, B.A.; Zahoor, M.; Ullah, R.; Khan, F.A.; Sultan, M.A. Modern Diagnostic Imaging Technique Applications and Risk Factors in the Medical Field: A Review. *Biomed Res Int* **2022**, *2022*, 5164970, doi:10.1155/2022/5164970.
2. Rong, J.; Liu, Y. Advances in Medical Imaging Techniques. *BMC Methods* **2024**, *1*, 10, s44330-024-00010–00017, doi:10.1186/s44330-024-00010-7.
3. Christensen-Jeffries, K.; Couture, O.; Dayton, P.A.; Eldar, Y.C.; Hynynen, K.; Kiessling, F.; O'Reilly, M.; Pinton, G.F.; Schmitz, G.; Tang, M.-X.; et al. Super-Resolution Ultrasound Imaging. *Ultrasound Med. Biol.* **2020**, *46*, 865–891, doi:10.1016/j.ultrasmedbio.2019.11.013.
4. Moran, C.M.; Thomson, A.J.W. Preclinical Ultrasound Imaging—A Review of Techniques and Imaging Applications. *Front. Phys.* **2020**, *8*, 124, doi:10.3389/fphy.2020.00124.
5. Trotter, J.; Pantel, A.R.; Teo, B.-K.K.; Escorcia, F.E.; Li, T.; Pryma, D.A.; Taunk, N.K. Positron Emission Tomography (PET)/Computed Tomography (CT) Imaging in Radiation Therapy Treatment Planning: A

 doi:10.20944/preprints202509.0352.v1

Review of PET Imaging Tracers and Methods to Incorporate PET/CT. *Adv. Radiat. Oncol.* **2023**, *8*, 101212, doi:10.1016/j.adro.2023.101212.

6. Moonen, C.T.W.; Van Zijl, P.C.M.; Frank, J.A.; Le Bihan, D.; Becker, E.D. Functional Magnetic Resonance Imaging in Medicine and Physiology. *Science* **1990**, *250*, 53–61, doi:10.1126/science.2218514.
7. La Fougère, C.; Rominger, A.; Förster, S.; Geisler, J.; Bartenstein, P. PET and SPECT in Epilepsy: A Critical Review. *Epilepsy & Behavior* **2009**, *15*, 50–55, doi:10.1016/j.yebeh.2009.02.025.
8. Panagiotopoulos, N.; Vogt, F.; Barkhausen, J.; Buzug, T.M.; Duschka, R.L.; Lüdtke-Buzug, K.; Ahlborg, M.; Bringout, G.; Debbeler, C.; Gräser, M.; et al. Magnetic Particle Imaging: Current Developments and Future Directions. *Int. J. Nanomedicine* **2015**, 3097, doi:10.2147/IJN.S70488.
9. Yang, X.; Shao, G.; Zhang, Y.; Wang, W.; Qi, Y.; Han, S.; Li, H. Applications of Magnetic Particle Imaging in Biomedicine: Advancements and Prospects. *Front. Physiol.* **2022**, *13*, 898426, doi:10.3389/fphys.2022.898426.
10. Gleich, B.; Weizenecker, J. Tomographic Imaging Using the Nonlinear Response of Magnetic Particles. *Nature* **2005**, *435*, 1214–1217, doi:10.1038/nature03808.
11. Ludwig, F.; Remmer, H.; Kuhlmann, C.; Wawrzik, T.; Arami, H.; Ferguson, R.M.; Krishnan, K.M. Self-Consistent Magnetic Properties of Magnetite Tracers Optimized for Magnetic Particle Imaging Measured by Ac Susceptometry, Magnetorelaxometry and Magnetic Particle Spectroscopy. *J. Magn. Magn. Mater.* **2014**, *360*, 169–173, doi:10.1016/j.jmmm.2014.02.020.
12. Xie, X.; Zhai, J.; Zhou, X.; Guo, Z.; Lo, P.; Zhu, G.; Chan, K.W.Y.; Yang, M. Magnetic Particle Imaging: From Tracer Design to Biomedical Applications in Vasculature Abnormality. *Adv. Mater.* **2024**, *36*, 2306450, doi:10.1002/adma.202306450.
13. Lu, C.; Han, L.; Wang, J.; Wan, J.; Song, G.; Rao, J. Engineering of Magnetic Nanoparticles as Magnetic Particle Imaging Tracers. *Chem. Soc. Rev.* **2021**, *50*, 8102–8146, doi:10.1039/D0CS00260G.
14. Song, G.; Chen, M.; Zhang, Y.; Cui, L.; Qu, H.; Zheng, X.; Wintermark, M.; Liu, Z.; Rao, J. Janus Iron Oxides @ Semiconducting Polymer Nanoparticle Tracer for Cell Tracking by Magnetic Particle Imaging. *Nano Lett.* **2018**, *18*, 182–189, doi:10.1021/acs.nanolett.7b03829.
15. Song, G.; Zheng, X.; Wang, Y.; Xia, X.; Chu, S.; Rao, J. A Magneto-Optical Nanoplatform for Multimodality Imaging of Tumors in Mice. *ACS Nano* **2019**, *13*, 7750–7758, doi:10.1021/acsnano.9b01436.
16. Chandrasekharan, P.; Tay, Z.W.; Hensley, D.; Zhou, X.Y.; Fung, B.K.; Colson, C.; Lu, Y.; Fellows, B.D.; Huynh, Q.; Saayujya, C.; et al. Using Magnetic Particle Imaging Systems to Localize and Guide Magnetic Hyperthermia Treatment: Tracers, Hardware, and Future Medical Applications. *Theranostics* **2020**, *10*, 2965–2981, doi:10.7150/thno.40858.
17. Talebloo, N.; Gudi, M.; Robertson, N.; Wang, P. Magnetic Particle Imaging: Current Applications in Biomedical Research. *J. Magn. Reson. Imaging* **2020**, *51*, 1659–1668, doi:10.1002/jmri.26875.
18. Tay, Z.W.; Chandrasekharan, P.; Chiu-Lam, A.; Hensley, D.W.; Dhavalikar, R.; Zhou, X.Y.; Yu, E.Y.; Goodwill, P.W.; Zheng, B.; Rinaldi, C.; et al. Magnetic Particle Imaging-Guided Heating in Vivo Using Gradient Fields for Arbitrary Localization of Magnetic Hyperthermia Therapy. *ACS Nano* **2018**, *12*, 3699–3713, doi:10.1021/acsnano.8b00893.
19. Goodwill, P.W.; Tamrazian, A.; Croft, L.R.; Lu, C.D.; Johnson, E.M.; Pidaparthi, R.; Ferguson, R.M.; Khandhar, A.P.; Krishnan, K.M.; Conolly, S.M. Ferrohydrodynamic Relaxometry for Magnetic Particle Imaging. *Appl. Phys. Lett.* **2011**, *98*, 262502, doi:10.1063/1.3604009.
20. Biederer, S.; Knopp, T.; Sattel, T.F.; Lüdtke-Buzug, K.; Gleich, B.; Weizenecker, J.; Borgert, J.; Buzug, T.M. Magnetization Response Spectroscopy of Superparamagnetic Nanoparticles for Magnetic Particle Imaging. *J. Phys. D: Appl. Phys.* **2009**, *42*, 205007, doi:10.1088/0022-3727/42/20/205007.
21. Tay, Z.W.; Goodwill, P.W.; Hensley, D.W.; Taylor, L.A.; Zheng, B.; Conolly, S.M. A High-Throughput, Arbitrary-Waveform, MPI Spectrometer and Relaxometer for Comprehensive Magnetic Particle Optimization and Characterization. *Sci. Rep.* **2016**, *6*, 34180, doi:10.1038/srep34180.
22. Liu, S.; Chiu-Lam, A.; Rivera-Rodriguez, A.; DeGroff, R.; Savliwala, S.; Sarna, N.; Rinaldi-Ramos, C.M. Long Circulating Tracer Tailored for Magnetic Particle Imaging. *Nanotheranostics* **2021**, *5*, 348–361, doi:10.7150/ntno.58548.

 doi:10.20944/preprints202509.0352.v1

23. Irfan, M.; Dogan, N.; Sapmaz, T.; Bingolbali, A. Development of MPI Relaxometer for Characterization of Superparamagnetic Nanoparticles. *Journal of Magnetism and Magnetic Materials* **2021**, *536*, 168082, doi:10.1016/j.jmmm.2021.168082.
24. Reimer, P.; Balzer, T. Ferucarbotran (Resovist): A New Clinically Approved RES-Specific Contrast Agent for Contrast-Enhanced MRI of the Liver: Properties, Clinical Development, and Applications. *Eur. Radiol.* **2003**, *13*, 1266–1276, doi:10.1007/s00330-002-1721-7.
25. Eberbeck, D.; Wiekhorst, F.; Wagner, S.; Trahms, L. How the Size Distribution of Magnetic Nanoparticles Determines Their Magnetic Particle Imaging Performance. *Applied Physics Letters* **2011**, *98*, 182502, doi:10.1063/1.3586776.
26. Avugadda, S.K.; Wickramasinghe, S.; Niculaes, D.; Ju, M.; Lak, A.; Silvestri, N.; Nitti, S.; Roy, I.; Samia, A.C.S.; Pellegrino, T. Uncovering the Magnetic Particle Imaging and Magnetic Resonance Imaging Features of Iron Oxide Nanocube Clusters. *Nanomaterials* **2020**, *11*, 62, doi:10.3390/nano11010062.
27. Good, H.J.; Sehl, O.C.; Gevaert, J.J.; Yu, B.; Berih, M.A.; Montero, S.A.; Rinaldi-Ramos, C.M.; Foster, P.J. Inter-User Comparison for Quantification of Superparamagnetic Iron Oxides with Magnetic Particle Imaging across Two Institutions Highlights a Need for Standardized Approaches 2023.
28. Gevaert, J.; Van Beek, K.; Sehl, O.C.; Foster, P.J. VivoTrax+ Improves the Detection of Cancer Cells with Magnetic Particle Imaging. *Int. J. Mag. Part. Imag.* **2022**, Vol 8 No 2 (2022), doi:10.18416/IJMPI.2022.2210001.
29. Nejadnik, H.; Pandit, P.; Lenkov, O.; Lahiji, A.P.; Yerneni, K.; Daldrup-Link, H.E. Ferumoxytol Can Be Used for Quantitative Magnetic Particle Imaging of Transplanted Stem Cells. *Mol. Imaging Biol.* **2019**, *21*, 465–472, doi:10.1007/s11307-018-1276-x.
30. Chandrasekharan, P.; Tay, Z.W.; Zhou, X.Y.; Yu, E.; Orendorff, R.; Hensley, D.; Huynh, Q.; Fung, K.L.B.; VanHook, C.C.; Goodwill, P.; et al. A Perspective on a Rapid and Radiation-Free Tracer Imaging Modality, Magnetic Particle Imaging, with Promise for Clinical Translation. *Br. J. Radiol* . **2018**, *91*, 20180326, doi:10.1259/bjr.20180326.
31. Vogel, P.; Kampf, T.; Rückert, M.; Grüttner, C.; Kowalski, A.; Teller, H.; Behr, V. Synomag®: The New High-Performance Tracer for Magnetic Particle Imaging. *Int. J. Mag. Part. Imag.* **2021**, Vol 7 No 1 (2021), doi:10.18416/IJMPI.2021.2103003.
32. Ferguson, R.M.; Khandhar, A.P.; Kemp, S.J.; Arami, H.; Saritas, E.U.; Croft, L.R.; Konkle, J.; Goodwill, P.W.; Halkola, A.; Rahmer, J.; et al. Magnetic Particle Imaging With Tailored Iron Oxide Nanoparticle Tracers. *IEEE Trans. Med. Imaging* **2015**, *34*, 1077–1084, doi:10.1109/TMI.2014.2375065.
33. Lawaczeck, R.; Bauer, H.; Frenzel, T.; Hasegawa, M.; Ito, Y.; Kito, K.; Miwa, N.; Tsutsui, H.; Vogler, H.; Weinmann, H.-J. Magnetic Iron Oxide Particles Coated with Carboxydextran for Parenteral Administration and Liver Contrasting: Pre-Clinical Profile of SH U555A. *Acta Radiol.* **1997**, *38*, 584–597, doi:10.1080/02841859709174391.
34. Balakrishnan, V.S.; Rao, M.; Kausz, A.T.; Brenner, L.; Pereira, B.J.G.; Frigo, T.B.; Lewis, J.M. Physicochemical Properties of Ferumoxytol, a New Intravenous Iron Preparation. *Eur. J. Clin. Investigation* **2009**, *39*, 489–496, doi:10.1111/j.1365-2362.2009.02130.x.
35. Rezaei, B.; Tay, Z.W.; Mostufa, S.; Manzari, O.N.; Azizi, E.; Ciannella, S.; Moni, H.-E.-J.; Li, C.; Zeng, M.; Gómez-Pastora, J.; et al. Magnetic Nanoparticles for Magnetic Particle Imaging (MPI): Design and Applications. *Nanoscale* **2024**, *16*, 11802–11824, doi:10.1039/D4NR01195C.
36. Lu, K.; Goodwill, P.; Zheng, B.; Conolly, S. Reshaping the 2D MPI PSF to Be Isotropic and Sharp Using Vector Acquisition and Equalization. In Proceedings of the 2015 5th International Workshop on Magnetic Particle Imaging (IWMPI); IEEE: Istanbul, Turkey, March 2015; pp. 1–1.
37. Ziemian, S.; Löwa, N.; Kosch, O.; Bajj, D.; Wiekhorst, F.; Schütz, G. Optimization of Iron Oxide Tracer Synthesis for Magnetic Particle Imaging. *Nanomaterials* **2018**, *8*, 180, doi:10.3390/nano8040180.
38. Wang, Q.; Ma, X.; Liao, H.; Liang, Z.; Li, F.; Tian, J.; Ling, D. Artificially Engineered Cubic Iron Oxide Nanoparticle as a High-Performance Magnetic Particle Imaging Tracer for Stem Cell Tracking. *ACS Nano* **2020**, *14*, 2053–2062, doi:10.1021/acsnano.9b08660.
39. Ferguson, R.M.; Khandhar, A.P.; Krishnan, K.M. Tracer Design for Magnetic Particle Imaging (Invited). *J. Appl. Phys* . **2012**, *111*, 07B318, doi:10.1063/1.3676053.

40. Tay, Z.W.; Hensley, D.W.; Vreeland, E.C.; Zheng, B.; Conolly, S.M. The Relaxation Wall: Experimental Limits to Improving MPI Spatial Resolution by Increasing Nanoparticle Core Size. *Biomed. Phys. Eng. Express* **2017**, *3*, 035003, doi:10.1088/2057-1976/aa6ab6.
41. Sehl, O.C.; Gevaert, J.J.; Melo, K.P.; Knier, N.N.; Foster, P.J. A Perspective on Cell Tracking with Magnetic Particle Imaging. *Tomography* **2020**, *6*, 315–324, doi:10.18383/j.tom.2020.00043.
42. Nigam, S.; Mohapatra, J.; Makela, A.V.; Hayat, H.; Rodriguez, J.M.; Sun, A.; Kenyon, E.; Redman, N.A.; Spence, D.; Jabin, G.; et al. Shape Anisotropy-Governed High-Performance Nanomagnetosol for In Vivo Magnetic Particle Imaging of Lungs. *Small* **2024**, *20*, 2305300, doi:10.1002/smll.202305300.
43. Juhong, A.; Li, B.; Liu, Y.; Yang, C.; Yao, C.; Agnew, D.W.; Lei, Y.L.; Luker, G.D.; Bumpers, H.; Huang, X.; et al. Multihead Attention U-Net for Magnetic Particle Imaging–Computed Tomography Image Segmentation. *Adv. Intell. Syst.* **2024**, *6*, 2400007, doi:10.1002/aisy.202400007.
44. Palchoudhury, S.; Xu, Y.; Goodwin, J.; Bao, Y. Synthesis of Iron Oxide Nanoworms. *Journal of Applied Physics* **2011**, *109*, 07E314, doi:10.1063/1.3549600.
45. Park, J.; Von Maltzahn, G.; Zhang, L.; Schwartz, M.P.; Ruoslahti, E.; Bhatia, S.N.; Sailor, M.J. Magnetic Iron Oxide Nanoworms for Tumor Targeting and Imaging. *Advanced Materials* **2008**, *20*, 1630–1635, doi:10.1002/adma.200800004.
46. Yang, C.-W.; Liu, K.; Yao, C.-Y.; Li, B.; Juhong, A.; Qiu, Z.; Huang, X. Indocyanine Green-Conjugated Superparamagnetic Iron Oxide Nanoworm for Multimodality Breast Cancer Imaging. *ACS Appl. Nano Mater.* **2022**, *5*, 18912–18920, doi:10.1021/acsanm.2c04687.
47. Tay, Z.W.; Savliwala, S.; Hensley, D.W.; Fung, K.L.B.; Colson, C.; Fellows, B.D.; Zhou, X.; Huynh, Q.; Lu, Y.; Zheng, B.; et al. Superferromagnetic Nanoparticles Enable Order-of-Magnitude Resolution & Sensitivity Gain in Magnetic Particle Imaging. *Small Methods* **2021**, *5*, 2100796, doi:10.1002/smtd.202100796.
48. Fung, K.L.B.; Colson, C.; Bryan, J.; Saayujya, C.; Mokkarala-Lopez, J.; Hartley, A.; Yousuf, K.; Kuo, R.; Lu, Y.; Fellows, B.D.; et al. First Superferromagnetic Remanence Characterization and Scan Optimization for Super-Resolution Magnetic Particle Imaging. *Nano Lett.* **2023**, *23*, 1717–1725, doi:10.1021/acs.nanolett.2c04404.
49. Zhao, Z.; Rinaldi, C. Computational Predictions of Enhanced Magnetic Particle Imaging Performance by Magnetic Nanoparticle Chains. *Phys. Med. Biol.* **2020**, *65*, 185013, doi:10.1088/1361-6560/ab95dd.
50. Kumar, P.P.P.; Nafiujjaman, M.; Makela, A.V.; Hadrick, K.; Hill, M.L.; Lee, M.; Kim, T. Development of Iron Oxide Nanochains as a Sensitive Magnetic Particle Imaging Tracer for Cancer Detection. *ACS Appl. Mater. Interfaces* **2025**, *17*, 20859–20871, doi:10.1021/acsami.5c00332.
51. Tomitaka, A.; Ota, S.; Nishimoto, K.; Arami, H.; Takemura, Y.; Nair, M. Dynamic Magnetic Characterization and Magnetic Particle Imaging Enhancement of Magnetic-Gold Core–Shell Nanoparticles. *Nanoscale* **2019**, *11*, 6489–6496, doi:10.1039/C9NR00242A.
52. Horvat, S.; Vogel, P.; Kampf, T.; Brandl, A.; Alshamsan, A.; Alhadlaq, H.A.; Ahamed, M.; Albrecht, K.; Behr, V.C.; Beilhack, A.; et al. Crosslinked Coating Improves the Signal-to-Noise Ratio of Iron Oxide Nanoparticles in Magnetic Particle Imaging (MPI). *Chem. NanoMat.* **2020**, *6*, 755–758, doi:10.1002/cnma.202000009.
53. Moor, L.; Scheibler, S.; Gerken, L.; Scheffler, K.; Thieben, F.; Knopp, T.; Herrmann, I.K.; Starsich, F.H.L. Particle Interactions and Their Effect on Magnetic Particle Spectroscopy and Imaging. *Nanoscale* **2022**, *14*, 7163–7173, doi:10.1039/D1NR08402J.
54. Duong, H.T.K.; Abdibastami, A.; Gloag, L.; Barrera, L.; Gooding, J.J.; Tilley, R.D. A Guide to the Design of Magnetic Particle Imaging Tracers for Biomedical Applications. *Nanoscale* **2022**, *14*, 13890–13914, doi:10.1039/D2NR01897G.
55. Azizi, E.; Rezaei, B.; Mostufa, S.; Liang, S.; Wang, Y.A.; Chugh, V.K.; Wang, J.-P.; Li, C.; Gómez-Pastora, J.; He, R.; et al. Effect of Tracer Size Distribution on Magnetic Particle Imaging Performance. *Phys. Scr.* **2025**, *100*, 025529, doi:10.1088/1402-4896/adab46.
56. Shasha, C.; Teeman, E.; Krishnan, K.M. Nanoparticle Core Size Optimization for Magnetic Particle Imaging. *Biomed. Phys. Eng. Express* **2019**, *5*, 055010, doi:10.1088/2057-1976/ab3972.

 doi:10.20944/preprints202509.0352.v1

57. Gloag, L.; Mehdipour, M.; Ulanova, M.; Mariandry, K.; Nichol, M.A.; Hernández-Castillo, D.J.; Gaudet, J.; Qiao, R.; Zhang, J.; Nelson, M.; et al. Zero Valent Iron Core–Iron Oxide Shell Nanoparticles as Small Magnetic Particle Imaging Tracers. *Chem. Commun.* **2020**, *56*, 3504–3507, doi:10.1039/C9CC08972A.
58. Seo, W.S.; Lee, J.H.; Sun, X.; Suzuki, Y.; Mann, D.; Liu, Z.; Terashima, M.; Yang, P.C.; McConnell, M.V.; Nishimura, D.G.; et al. FeCo/Graphitic-Shell Nanocrystals as Advanced Magnetic-Resonance-Imaging and near-Infrared Agents. *Nature Mater.* **2006**, *5*, 971–976, doi:10.1038/nmat1775.
59. Liu, J.; Wu, K.; Wang, J.-P. Magnetic Properties of Cubic FeCo Nanoparticles with Anisotropic Long Chain Structure. *AIP Advances* **2016**, *6*, 056126, doi:10.1063/1.4945042.
60. Song, G.; Kenney, M.; Chen, Y.-S.; Zheng, X.; Deng, Y.; Chen, Z.; Wang, S.X.; Gambhir, S.S.; Dai, H.; Rao, J. Carbon-Coated FeCo Nanoparticles as Sensitive Magnetic-Particle-Imaging Tracers with Photothermal and Magnetothermal Properties. *Nat. Biomed. Eng.* **2020**, *4*, 325–334, doi:10.1038/s41551-019-0506-0.
61. Wu, X.W.; Guslienko, K.Y.; Chantrell, R.W.; Weller, D. Magnetic Anisotropy and Thermal Stability Study on FePt Nanoparticle Assembly. *Appl. Phys. Lett.* **2003**, *82*, 3475–3477, doi:10.1063/1.1576501.
62. Yu, J.; Yang, C.; Li, J.; Ding, Y.; Zhang, L.; Yousaf, M.Z.; Lin, J.; Pang, R.; Wei, L.; Xu, L.; et al. Multifunctional Fe_5C_2 Nanoparticles: A Targeted Theranostic Platform for Magnetic Resonance Imaging and Photoacoustic Tomography-Guided Photothermal Therapy. *Advanced Materials* **2014**, *26*, 4114–4120, doi:10.1002/adma.201305811.
63. Silvestri, N.; Gavilán, H.; Guardia, P.; Brescia, R.; Fernandes, S.; Samia, A.C.S.; Teran, F.J.; Pellegrino, T. Di- and Tri-Component Spinel Ferrite Nanocubes: Synthesis and Their Comparative Characterization for Theranostic Applications. *Nanoscale* **2021**, *13*, 13665–13680, doi:10.1039/D1NR01044A.
64. Bauer, L.M.; Situ, S.F.; Griswold, M.A.; Samia, A.C.S. High-Performance Iron Oxide Nanoparticles for Magnetic Particle Imaging – Guided Hyperthermia (hMPI). *Nanoscale* **2016**, *8*, 12162–12169, doi:10.1039/C6NR01877G.
65. Jiang, Z.; Han, X.; Du, Y.; Li, Y.; Li, Y.; Li, J.; Tian, J.; Wu, A. Mixed Metal Metal–Organic Frameworks Derived Carbon Supporting $ZnFe_2O_4$ /C for High-Performance Magnetic Particle Imaging. *Nano Lett.* **2021**, *21*, 2730–2737, doi:10.1021/acs.nanolett.0c04455.
66. Kratz, H.; Mohtashamdolatshahi, A.; Eberbeck, D.; Kosch, O.; Wiekhorst, F.; Taupitz, M.; Hamm, B.; Stolzenburg, N.; Schnorr, J. Tailored Magnetic Multicore Nanoparticles for Use as Blood Pool MPI Tracers. *Nanomaterials* **2021**, *11*, 1532, doi:10.3390/nano11061532.
67. Kratz, H.; Taupitz, M.; Ariza De Schellenberger, A.; Kosch, O.; Eberbeck, D.; Wagner, S.; Trahms, L.; Hamm, B.; Schnorr, J. Novel Magnetic Multicore Nanoparticles Designed for MPI and Other Biomedical Applications: From Synthesis to First in Vivo Studies. *PLoS ONE* **2018**, *13*, e0190214, doi:10.1371/journal.pone.0190214.
68. Makela, A.V.; Schott, M.A.; Madsen, C.S.; Greeson, E.M.; Contag, C.H. Magnetic Particle Imaging of Magnetotactic Bacteria as Living Contrast Agents Is Improved by Altering Magnetosome Arrangement. *Nano Lett.* **2022**, *22*, 4630–4639, doi:10.1021/acs.nanolett.1c05042.
69. Zhu, X.; Li, J.; Peng, P.; Hosseini Nassab, N.; Smith, B.R. Quantitative Drug Release Monitoring in Tumors of Living Subjects by Magnetic Particle Imaging Nanocomposite. *Nano Lett.* **2019**, *19*, 6725–6733, doi:10.1021/acs.nanolett.9b01202.
70. Antonelli, A.; Szwargulski, P.; Scarpa, E.-S.; Thieben, F.; Cordula, G.; Ambrosi, G.; Guidi, L.; Ludewig, P.; Knopp, T.; Magnani, M. Development of Long Circulating Magnetic Particle Imaging Tracers: Use of Novel Magnetic Nanoparticles and Entrapment Into Human Erythrocytes. *Nanomedicine (Lond.)* **2020**, *15*, 739–753, doi:10.2217/nnm-2019-0449.
71. Hildebrand, S.; Löwa, N.; Paysen, H.; Fratila, R.M.; Reverte-Salisa, L.; Trakoolwilaiwan, T.; Niu, Z.; Kasparis, G.; Preuss, S.F.; Kosch, O.; et al. Quantification of Lipoprotein Uptake in Vivo Using Magnetic Particle Imaging and Spectroscopy. *ACS Nano* **2021**, *15*, 434–446, doi:10.1021/acsnano.0c03229.
72. Harvell-Smith, S.; Tung, L.D.; Thanh, N.T.K. Magnetic Particle Imaging: Tracer Development and the Biomedical Applications of a Radiation-Free, Sensitive, and Quantitative Imaging Modality. *Nanoscale* **2022**, *14*, 3658–3697, doi:10.1039/D1NR05670K.

73. Lindemann, A.; Fraederich, B.M.; Pries, R.; Wollenberg, B.; Lüdtke-Buzug, K.; Graefe, K. Biological Impact of Superparamagnetic Iron Oxide Nanoparticles for Magnetic Particle Imaging of Head and Neck Cancer Cells. *Int. J. Nanomedicine* **2014**, 5025, doi:10.2147/IJN.S63873.
74. Gandhi, S.; Arami, H.; Krishnan, K.M. Detection of Cancer-Specific Proteases Using Magnetic Relaxation of Peptide-Conjugated Nanoparticles in Biological Environment. *Nano Lett.* **2016**, *16*, 3668–3674, doi:10.1021/acs.nanolett.6b00867.
75. Melo, K.P.; Makela, A.V.; Knier, N.N.; Hamilton, A.M.; Foster, P.J. Magnetic Microspheres Can Be Used for Magnetic Particle Imaging of Cancer Cells Arrested in the Mouse Brain. *Magnetic Resonance in Med* **2022**, *87*, 312–322, doi:10.1002/mrm.28987.
76. Parkins, K.M.; Melo, K.P.; Chen, Y.; Ronald, J.A.; Foster, P.J. Visualizing Tumour Self-Homing with Magnetic Particle Imaging. *Nanoscale* **2021**, *13*, 6016–6023, doi:10.1039/D0NR07983A.
77. Zheng, B.; Vazin, T.; Goodwill, P.W.; Conway, A.; Verma, A.; Ulku Saritas, E.; Schaffer, D.; Conolly, S.M. Magnetic Particle Imaging Tracks the Long-Term Fate of in Vivo Neural Cell Implants with High Image Contrast. *Sci Rep* **2015**, *5*, 14055, doi:10.1038/srep14055.
78. Makela, A.V.; Gaudet, J.M.; Foster, P.J. Quantifying Tumor Associated Macrophages in Breast Cancer: A Comparison of Iron and Fluorine-Based MRI Cell Tracking. *Sci. Rep.* **2017**, *7*, 42109, doi:10.1038/srep42109.
79. Makela, A.V.; Foster, P.J. Imaging Macrophage Distribution and Density in Mammary Tumors and Lung Metastases Using Fluorine-19 MRI Cell Tracking. *Magnetic Resonance in Med.* **2018**, *80*, 1138–1147, doi:10.1002/mrm.27081.
80. Makela, A.V.; Gaudet, J.M.; Schott, M.A.; Sehl, O.C.; Contag, C.H.; Foster, P.J. Magnetic Particle Imaging of Macrophages Associated with Cancer: Filling the Voids Left by Iron-Based Magnetic Resonance Imaging. *Mol. Imaging Biol.* **2020**, *22*, 958–968, doi:10.1007/s11307-020-01473-0.
81. Gerosa, M.; Ren, G.; Zhang, Y.; Goodwill, P.; Mansfield, J.; Marzola, P.; Wintermark, M. Preliminary Results: Imaging of in Situ Labeled Tumor-Associated Macrophages with Magnetic Particle Imaging. *Int. J. Magn. Part. Imaging* **2020**, Vol 6 No 2 Suppl. 1 (2020), doi:10.18416/IJMPI.2020.2009029.
82. Gaudet, J.; Mansfield, J.; Goodwill, P. Imaging Cancer Immunology: Tracking Immune Cells in Vivo with Magnetic Particle Imaging. *J. Immunol.* **2019**, *202*, 130.7-130.7, doi:10.4049/jimmunol.202.Supp.130.7.
83. Rivera-Rodriguez, A.; Hoang-Minh, L.B.; Chiu-Lam, A.; Sarna, N.; Marrero-Morales, L.; Mitchell, D.A.; Rinaldi-Ramos, C.M. Tracking Adoptive T Cell Immunotherapy Using Magnetic Particle Imaging. *Nanotheranostics* **2021**, *5*, 431–444, doi:10.7150/ntno.55165.
84. Gevaert, J.J.; Fink, C.; Dikeakos, J.D.; Dekaban, G.A.; Foster, P.J. Magnetic Particle Imaging Is a Sensitive In Vivo Imaging Modality for the Detection of Dendritic Cell Migration. *Mol. Imaging Biol.* **2022**, *24*, 886–897, doi:10.1007/s11307-022-01738-w.
85. Lefevre, S.; Ruimy, D.; Jehl, F.; Neuville, A.; Robert, P.; Sordet, C.; Ehlinger, M.; Dietemann, J.-L.; Bierry, G. Septic Arthritis: Monitoring with USPIO-Enhanced Macrophage MR Imaging. *Radiology* **2011**, *258*, 722–728, doi:10.1148/radiol.10101272.
86. Ruehm, S.G.; Corot, C.; Vogt, P.; Kolb, S.; Debatin, J.F. Magnetic Resonance Imaging of Atherosclerotic Plaque With Ultrasmall Superparamagnetic Particles of Iron Oxide in Hyperlipidemic Rabbits. *Circulation* **2001**, *103*, 415–422, doi:10.1161/01.CIR.103.3.415.
87. Tong, W.; Hui, H.; Shang, W.; Zhang, Y.; Tian, F.; Ma, Q.; Yang, X.; Tian, J.; Chen, Y. Highly Sensitive Magnetic Particle Imaging of Vulnerable Atherosclerotic Plaque with Active Myeloperoxidase-Targeted Nanoparticles. *Theranostics* **2021**, *11*, 506–521, doi:10.7150/thno.49812.
88. Chandrasekharan, P.; Fung, K.L.B.; Zhou, X.Y.; Cui, W.; Colson, C.; Mai, D.; Jeffris, K.; Huynh, Q.; Saayujya, C.; Kabuli, L.; et al. Non-Radioactive and Sensitive Tracking of Neutrophils towards Inflammation Using Antibody Functionalized Magnetic Particle Imaging Tracers. *Nanotheranostics* **2021**, *5*, 240–255, doi:10.7150/ntno.50721.
89. Remmo, A.; Löwa, N.; Kosch, O.; Eberbeck, D.; Ludwig, A.; Kampen, L.; Grüttner, C.; Wiekhorst, F. Cell Tracking by Magnetic Particle Imaging: Methodology for Labeling THP-1 Monocytes with Magnetic Nanoparticles for Cellular Imaging. *Cells* **2022**, *11*, 2892, doi:10.3390/cells11182892.
90. Mangarova, D.B.; Brangsch, J.; Mohtashamdolatshahi, A.; Kosch, O.; Paysen, H.; Wiekhorst, F.; Klopfleisch, R.; Buchholz, R.; Karst, U.; Taupitz, M.; et al. Ex Vivo Magnetic Particle Imaging of Vascular Inflammation

in Abdominal Aortic Aneurysm in a Murine Model. *Sci. Rep.* **2020**, *10*, 12410, doi:10.1038/s41598-020-69299-y.

91. Alzahrani, E.O.; Asiri, A.; El-Dessoky, M.M.; Kuang, Y. Quiescence as an Explanation of Gompertzian Tumor Growth Revisited. *Mathematical Biosciences* **2014**, *254*, 76–82, doi:10.1016/j.mbs.2014.06.009.
92. Arami, H.; Teeman, E.; Troksa, A.; Bradshaw, H.; Saatchi, K.; Tomitaka, A.; Gambhir, S.S.; Häfeli, U.O.; Liggitt, D.; Krishnan, K.M. Tomographic Magnetic Particle Imaging of Cancer Targeted Nanoparticles. *Nanoscale* **2017**, *9*, 18723–18730, doi:10.1039/C7NR05502A.
93. Lin, Z.; Ding, J.; Sun, G.; Li, D.; He, S.; Liang, X.; Huang, X.; Xie, J. Application of Paclitaxel-Loaded EGFR Peptide-Conjugated Magnetic Polymeric Liposomes for Liver Cancer Therapy. *Curr. Med. Sci.* **2020**, *40*, 145–154, doi:10.1007/s11596-020-2158-4.
94. Yu, E.Y.; Bishop, M.; Zheng, B.; Ferguson, R.M.; Khandhar, A.P.; Kemp, S.J.; Krishnan, K.M.; Goodwill, P.W.; Conolly, S.M. Magnetic Particle Imaging: A Novel in Vivo Imaging Platform for Cancer Detection. *Nano Lett.* **2017**, *17*, 1648–1654, doi:10.1021/acs.nanolett.6b04865.
95. Meng, L.; Ma, X.; Jiang, S.; Ji, G.; Han, W.; Xu, B.; Tian, J.; Tian, W. High-Efficiency Fluorescent and Magnetic Multimodal Probe for Long-Term Monitoring and Deep Penetration Imaging of Tumors. *J. Mater. Chem. B* **2019**, *7*, 5345–5351, doi:10.1039/C9TB00638A.
96. You, H.; Shang, W.; Min, X.; Weinreb, J.; Li, Q.; Leapman, M.; Wang, L.; Tian, J. Sight and Switch off: Nerve Density Visualization for Interventions Targeting Nerves in Prostate Cancer. *Sci. Adv.* **2020**, *6*, eaax6040, doi:10.1126/sciadv.aax6040.
97. Bai, S.; Gai, L.; Zhang, Q.; Kang, Y.; Liu, Z.; He, Y.; Liu, W.; Jiang, T.; Du, Z.; Du, S.; et al. Development of a Human-Size Magnetic Particle Imaging Device for Sentinel Lymph Node Biopsy of Breast Cancer. *Front. Bioeng. Biotechnol.* **2024**, *12*, 1327521, doi:10.3389/fbioe.2024.1327521.
98. Yang, C.-W.; Liu, K.; Yao, C.-Y.; Li, B.; Juhong, A.; Ullah, A.K.M.A.; Bumpers, H.; Qiu, Z.; Huang, X. Active Targeting Hyaluronan Conjugated Nanoprobe for Magnetic Particle Imaging and Near-Infrared Fluorescence Imaging of Breast Cancer and Lung Metastasis. *ACS Appl. Mater. Interfaces* **2024**, *16*, 27055–27064, doi:10.1021/acsami.4c01623.
99. Fuller, E.G.; Scheutz, G.M.; Jimenez, A.; Lewis, P.; Savliwala, S.; Liu, S.; Sumerlin, B.S.; Rinaldi, C. Theranostic Nanocarriers Combining High Drug Loading and Magnetic Particle Imaging. *International Journal of Pharmaceutics* **2019**, *572*, 118796, doi:10.1016/j.ijpharm.2019.118796.
100. Tomitaka, A.; Arami, H.; Ahmadivand, A.; Pala, N.; McGoron, A.J.; Takemura, Y.; Febo, M.; Nair, M. Magneto-Plasmonic Nanostars for Image-Guided and NIR-Triggered Drug Delivery. *Sci. Rep.* **2020**, *10*, 10115, doi:10.1038/s41598-020-66706-2.
101. Toomajian, V.A.; Tundo, A.; Ural, E.E.; Greeson, E.M.; Contag, C.H.; Makela, A.V. Magnetic Particle Imaging Reveals That Iron-Labeled Extracellular Vesicles Accumulate in Brains of Mice with Metastases. *ACS Appl. Mater. Interfaces* **2024**, *16*, 30860–30873, doi:10.1021/acsami.4c04920.
102. Jia, G.; Han, Y.; An, Y.; Ding, Y.; He, C.; Wang, X.; Tang, Q. NRP-1 Targeted and Cargo-Loaded Exosomes Facilitate Simultaneous Imaging and Therapy of Glioma in Vitro and in Vivo. *Biomaterials* **2018**, *178*, 302–316, doi:10.1016/j.biomaterials.2018.06.029.
103. Jung, K.O.; Jo, H.; Yu, J.H.; Gambhir, S.S.; Pratx, G. Development and MPI Tracking of Novel Hypoxia-Targeted Theranostic Exosomes. *Biomaterials* **2018**, *177*, 139–148, doi:10.1016/j.biomaterials.2018.05.048.
104. Liu, X.; Zhang, Y.; Wang, Y.; Zhu, W.; Li, G.; Ma, X.; Zhang, Y.; Chen, S.; Tiwari, S.; Shi, K.; et al. Comprehensive Understanding of Magnetic Hyperthermia for Improving Antitumor Therapeutic Efficacy. *Theranostics* **2020**, *10*, 3793–3815, doi:10.7150/thno.40805.
105. Buchholz, O.; Sajjamark, K.; Franke, J.; Wei, H.; Behrends, A.; Münkel, C.; Grüttner, C.; Levan, P.; Von Elverfeldt, D.; Graeser, M.; et al. In Situ Theranostic Platform Combining Highly Localized Magnetic Fluid Hyperthermia, Magnetic Particle Imaging, and Thermometry in 3D. *Theranostics* **2024**, *14*, 324–340, doi:10.7150/thno.86759.
106. Bleul, R.; Baki, A.; Freese, C.; Paysen, H.; Kosch, O.; Wiekhorst, F. Continuously Manufactured Single-Core Iron Oxide Nanoparticles for Cancer Theranostics as Valuable Contribution in Translational Research. *Nanoscale Adv.* **2020**, *2*, 4510–4521, doi:10.1039/D0NA00343C.

107. Du, Y.; Liu, X.; Liang, Q.; Liang, X.-J.; Tian, J. Optimization and Design of Magnetic Ferrite Nanoparticles with Uniform Tumor Distribution for Highly Sensitive MRI/MPI Performance and Improved Magnetic Hyperthermia Therapy. *Nano Lett.* **2019**, *19*, 3618–3626, doi:10.1021/acs.nanolett.9b00630.
108. Jordan, A.; Scholz, R.; Wust, P.; Schirra, H.; Thomas Schiestel; Schmidt, H.; Felix, R. Endocytosis of Dextran and Silan-Coated Magnetite Nanoparticles and the Effect of Intracellular Hyperthermia on Human Mammary Carcinoma Cells in Vitro. *Journal of Magnetism and Magnetic Materials* **1999**, *194*, 185–196, doi:10.1016/S0304-8853(98)00558-7.
109. Liu, X.L.; Fan, H.M.; Yi, J.B.; Yang, Y.; Choo, E.S.G.; Xue, J.M.; Fan, D.D.; Ding, J. Optimization of Surface Coating on Fe3O4 Nanoparticles for High Performance Magnetic Hyperthermia Agents. *J. Mater. Chem.* **2012**, *22*, 8235, doi:10.1039/c2jm30472d.
110. Khurshid, H.; Alonso, J.; Nemati, Z.; Phan, M.H.; Mukherjee, P.; Fdez-Gubieda, M.L.; Barandiarán, J.M.; Srikanth, H. Anisotropy Effects in Magnetic Hyperthermia: A Comparison between Spherical and Cubic Exchange-Coupled FeO/Fe3O4 Nanoparticles. *J. Appl. Phys* . **2015**, *117*, 17A337, doi:10.1063/1.4919250.
111. Mason, E.E.; Mattingly, E.; Herb, K.; Śliwiak, M.; Franconi, S.; Cooley, C.Z.; Slanetz, P.J.; Wald, L.L. Concept for Using Magnetic Particle Imaging for Intraoperative Margin Analysis in Breast-Conserving Surgery. *Sci Rep* **2021**, *11*, 13456, doi:10.1038/s41598-021-92644-8.
112. Azargoshasb, S.; Molenaar, L.; Rosiello, G.; Buckle, T.; Van Willigen, D.M.; Van De Loosdrecht, M.M.; Welling, M.M.; Alic, L.; Van Leeuwen, F.W.B.; Winter, A.; et al. Advancing Intraoperative Magnetic Tracing Using 3D Freehand Magnetic Particle Imaging. *Int. J. Comput.Assist. Radiol. Surg.* **2022**, *17*, 211–218, doi:10.1007/s11548-021-02458-2.
113. Liu, J.F.; Neel, N.; Dang, P.; Lamb, M.; McKenna, J.; Rodgers, L.; Litt, B.; Cheng, Z.; Tsourkas, A.; Issadore, D. Radiofrequency-Triggered Drug Release from Nanoliposomes with Millimeter-Scale Resolution Using a Superimposed Static Gating Field. *Small* **2018**, *14*, 1802563, doi:10.1002/smll.201802563.
114. S, M. Development of Magnetic Nanocarriers Based on Thermosensitive Liposomes and Their Visualization Using Magnetic Particle Imaging. *Int. J. Nanomed. Nanosurg.* **2016**, *2*, doi:10.16966/2470-3206.111.
115. Rost, N.C.V.; Sen, K.; Savliwala, S.; Singh, I.; Liu, S.; Unni, M.; Raniero, L.; Rinaldi, C. Magnetic Particle Imaging Performance of Liposomes Encapsulating Iron Oxide Nanoparticles. *J. Magn. Magn. Mater.* **2020**, *504*, 166675, doi:10.1016/j.jmmm.2020.166675.
116. Fuller, E.G.; Sun, H.; Dhavalikar, R.D.; Unni, M.; Scheutz, G.M.; Sumerlin, B.S.; Rinaldi, C. Externally Triggered Heat and Drug Release from Magnetically Controlled Nanocarriers. *ACS Appl. Polym. Mater.* **2019**, *1*, 211–220, doi:10.1021/acsapm.8b00100.
117. Nigam, S.; Gjelaj, E.; Wang, R.; Wei, G.; Wang, P. Machine Learning and Deep Learning Applications in Magnetic Particle Imaging. *Magnetic Resonance Imaging* **2025**, *61*, 42–51, doi:10.1002/jmri.29294.
118. Hayat, H.; Sun, A.; Hayat, H.; Liu, S.; Talebloo, N.; Pinger, C.; Bishop, J.O.; Gudi, M.; Dwan, B.F.; Ma, X.; et al. Artificial Intelligence Analysis of Magnetic Particle Imaging for Islet Transplantation in a Mouse Model. *Mol. Imaging Biol.* **2021**, *23*, 18–29, doi:10.1007/s11307-020-01533-5.
119. Sun, A.; Hayat, H.; Liu, S.; Tull, E.; Bishop, J.O.; Dwan, B.F.; Gudi, M.; Talebloo, N.; Dizon, J.R.; Li, W.; et al. 3D in Vivo Magnetic Particle Imaging of Human Stem Cell-Derived Islet Organoid Transplantation Using a Machine Learning Algorithm. *Front. Cell Dev. Biol.* **2021**, *9*, 704483, doi:10.3389/fcell.2021.704483.
120. Dittmer, S.; Kluth, T.; Henriksen, M.T.R.; Maass, P. Deep Image Prior for 3D Magnetic Particle Imaging: A Quantitative Comparison of Regularization Techniques on Open MPI Dataset 2020.
121. Yin, L.; Guo, H.; Zhang, P.; Li, Y.; Hui, H.; Du, Y.; Tian, J. System Matrix Recovery Based on Deep Image Prior in Magnetic Particle Imaging. *Phys. Med. Biol.* **2023**, *68*, 035006, doi:10.1088/1361-6560/acaf47.
122. Dittmer, S.; Kluth, T.; Baguer, D.O.; Maass, P. A Deep Prior Approach to Magnetic Particle Imaging. In *Machine Learning for Medical Image Reconstruction*; Deeba, F., Johnson, P., Würfl, T., Ye, J.C., Eds.; Lecture Notes in Computer Science; Springer International Publishing: Cham, 2020; Vol. 12450, pp. 113–122 ISBN 978-3-030-61597-0.
123. Gungor, A.; Askin, B.; Soydan, D.A.; Baris Top, C.; Cukur, T. Deep Learned Super Resolution of System Matrices for Magnetic Particle Imaging. In Proceedings of the 2021 43rd Annual International Conference

 doi:10.20944/preprints202509.0352.v1

of the IEEE Engineering in Medicine & Biology Society (EMBC); IEEE: Mexico, November 1 2021; pp. 3749–3752.